Department of Physics and Astronomy
University of Heidelberg

Bachelor Thesis in Physics

submitted by

Alexander Lukas Wagner
born in Munich, Germany

2018

Topology in 1D quantum walks

This Bachelor Thesis has been carried out by

Alexander Lukas Wagner

at the Institute for Theoretical Physics Heidelberg
under the supervision of

Prof. Dr. Sandro Wimberger

Abstract

The application of topological concepts rooted in mathematics to physical systems has proven to be very useful, for example in the context of the quantum Hall effect. Among the powerful tools provided by topology is the Bulk-Edge-Correspondence, which draws a connection between protected states forming at the edge or rather the boundary of the system and the topological properties of its bulk, that is unaffected by boundary effects. In this work we study how the Bulk-Edge-Correspondence manifests itself for the double kicked quantum rotor and analyse how reliably (with regards to experimental perturbations) the observable mean chiral displacement converges towards the topological invariant of the system in the winding number.
Laying the groundwork for these considerations is the previous examination of the quantum kicked rotor model, especially the resonant and antiresonant configurations of the kicked rotor are highlighted. A new approach to the antiresonant configuration, charaterised through the use of a transformed Hamiltonian, is presented.

Die Anwendung topologischer Konzepte aus der Mathematik auf physikalische System hat sich als sehr nützlich herausgestellt, zum Beispiel bei der Erklärung des Quanten-Hall-Effekts. Eines der mächtigen, in der Topologie begründeten, Werkzeuge ist die "Bulk-Edge-Correspondence", welche eine Verbindung zwischen geschützten Randzuständen und den topologischen Eigenschaften des, von Randeffekten unbeeinflussten, Großteil eines Systems herstellt. Hauptaugenmerk dieser Arbeit ist die Untersuchung der "Bulk-Edge-Correspondence" für den "double kicked quantum rotor" und die Überprüfung der Konvergenz (auch unter experimentellen Störungen) des beobachtbaren "mean chiral displacement" gegen die topologische Invariante des Systems, die Windungszahl.
Vorausgehend werden die benötigten Grundlagen bei der Betrachtung des "quantum kicked rotor model" herausgearbeitet. Verstärkt werden die resonante und antiresonante Konfiguration des "quantum kicked rotor" hervorgehoben und für die antiresonante Konfiguration wird ein neuer Ansatz, beruhend auf einem transformierten Hamiltonoperator, vorgestellt.

Contents

Introduction

Motivation

In the domain of quantum computation, communication and cryptography experimentalists are struggling with the fundamental issue of decoherence, ever since work in the field has begun. Perfectly isolated quantum mechanical systems are impossible to realise, therefore unwanted perturbations and the decoherence they can cause have represented an unavoidable limiting factor on the experimental side of quantum information science. However, the discovery of topological phases [13] and their application to so-called "topological insulators" has revealed topologically protected edge states, that are unsensitive to large class of perturbations. The stability of these states is grounded in the Bulk-Edge-Correspondence imprinting the stability of the topological invariant on the edge states. Consequently, topological insulators might play a vital role in defying decoherence in future experiments.
The integer quantum Hall effect [12] is an instructive example for the exceptional stability of topological phases, that was previously mentioned. Topologically protected conducting edge states of an otherwise insulating bulk, explain the unsensitivity of the quantized plateaus in the Hall conductance.
In this work we will focus on the novel field of Floquet topological insulators, where the theory of topological phases is applied to periodically driven systems, namely the double kicked quantum rotor in our case. This approach is promising, because periodically driven systems are inherently susceptive to perturbative effects and the robustness of topological behaviour can help mitigate this issue. Moreover, new topological properties specific to periodically driven systems might emerge.

Outline

In chapter one the quantum kicked rotor model is introduced. With the explanation of quantum resonance, antiresonance and the experimental implementation the fundamentals for the following chapters are established.

In chapter two quantum random walks and their implementation in kicked rotor model are discussed. A comparison between ideal quantum walks and QKR walks is drawn.

Chapter three serves as a compilation of the concepts surrounding the study of topological phases. Among the most important ones are the sublattice symmetry and the Bulk-Edge-Correspondence.

In chapter four the topological classification of the double kicked quantum rotor is analysed. We check how reliably the observable mean chiral displacement converges towards the topological invariant of the system in the winding number under perturbations typically encountered in experiments.

Chapter 1

Quantum Kicked Rotor

1.1 Theory

In this first chapter we will discuss the Quantum Kicked Rotor (QKR for short), the following chapters will build on the ground work laid here. Let us consider a particle described by quantum mechanics and make it the subject of the kicked rotor potential. The Hamiltonian is given by:

$$\hat{H} = \frac{\hat{p}^2}{2} + k \cdot \cos\left(\hat{\theta}\right) \cdot \sum_{n=0}^{\infty} \delta(t - n\tau) \tag{1.1}$$
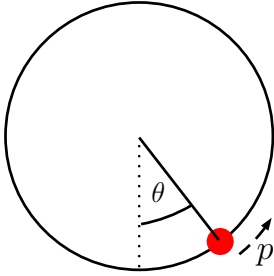
Figure 1.1: QKR

Notice that we are using a rescaled, unitfree version of the Hamiltonian, for more detail on the rescaling see subsection A.1.1. From equation (1.1) we immediately see that the Hamiltonian is periodic in time: $\hat{H}(t) = \hat{H}(t + \tau)$

This insight motivates us to calculate the time evolution operator for one period τ, which is also known as the Floquet operator. Departing from the Schrödinger equation for a time dependent Hamiltonian, we have to consider the Dyson series. Where $\hat{T}$ is the time ordering operator:

$$\hat{U}(t + \tau, t) = \hat{T} \exp\left(-i \int_t^{t+\tau} \hat{H}(t')dt'\right) \tag{1.2}$$

For simplicity's sake let us choose $t = 0$ and rewrite (1.2) as a product:

$$
\begin{aligned}
\hat{U}(\tau, 0) =& \hat{U}_{(\tau,\delta\tau)} \cdot \hat{U}_{[\delta\tau,0]} = \lim_{\delta\tau \to 0} \hat{U}_{(\tau,\delta\tau)} \cdot \hat{U}_{[\delta\tau,0]} \\
=& \lim_{\delta\tau \to 0} \hat{T} \exp\left(-i \int_{(\tau,\delta\tau)} \hat{H}(t')dt'\right) \lim_{\delta\tau \to 0} \hat{T} \exp\left(-i \int_{[\delta\tau,0]} \hat{H}(t')dt'\right) \\
=& \exp\left(-i\frac{\hat{p}^2}{2}\tau\right) \cdot \exp\left(-ik \cos\left(\hat{\theta}\right)\right) \tag{1.3}
\end{aligned}
$$

We used that the limits converge separately and that $\hat{T}$ commutes with $\lim_{\delta\tau \to 0}$, because taking the limit does not change time ordering.

1.1.1   Bloch theory

Now we will consider a one dimensional chain composed of subsequent copies of the system discussed previously (mapping figure 1.1 to a line segment). This means that the potential in question is periodic in position space and therefore Bloch's theorem applies.

The period of the potential is chosen to be 2π, to ensure consistency with the previous derivation (1.3), if we define:

$$\hat{\theta} = \hat{x} \mod 2\pi \tag{1.4}$$

The Bloch theorem provides us with a basis of solutions for the Schrödinger equation and every wavefunction ψ in this basis can be written as follows:

$$\psi(x,t) = e^{-i\beta x}\psi_\beta(x,t) \tag{1.5}$$

Here $\psi_\beta(x,t)$ is a periodic function in position space with the same period as the potential, namely 2π. Moreover Bloch's theorem implies, that momenta have to be quantised and the momentum operator takes on the following form:

$$\hat{p} = \hat{n} + \beta \tag{1.6}$$

In equation (1.6) the momentum is composed of $\beta \in [0,1)$ the quasi- or crystal momentum, which is conserved and an integer part n, which can vary in integer steps.
Applying this consideration to (1.3) leaves us with:

$$\hat{U} = \exp\left(-i\frac{(\hat{n}+\beta)^2}{2}\tau\right) \cdot \exp\left(-ik\cos\left(\hat{\theta}\right)\right) \tag{1.7}$$

1.1.2   Quantum Resonance

If we choose the time period τ and the quasimomentum β in such a way, that the free evolution part of the Floquet operator is equal to unity, the system is said to be in quantum resonance. In this case the free evolution does not alter the wavefunction and the time evolution is described exclusively by the kicks. The Floquet operator in quantum resonance simplifies to:

$$\hat{U} = e^{-ik\cos\left(\hat{\theta}\right)} \tag{1.8}$$

Quantum resonance is achieved for the combinations of β and τ listed below, departing from the condition:

$$\exp\left(-i\frac{\tau}{2}(\hat{n}+\beta)^2\right) \equiv \exp\left(-i\frac{\tau}{2}\left(\hat{n}^2 + 2\hat{n}\beta\right)\right) \stackrel{!}{\equiv} \mathbb{1} \tag{1.9}$$

In the first step the condition has been rewritten, neglecting the global phase. If we choose $\tau = 2\pi l$ for $l \in \mathbb{N}$, then in resonance β has to fulfill:

$$\beta = \frac{1}{2} + \frac{i}{l} \quad (\text{mod } 1) \qquad\qquad i \in \{0, ..., l-1\} \qquad (1.10)$$

The case where $\beta = 0$ and $\tau = 4\pi$ can be considered the simplest example of resonance. A rigorous derivation of (1.10) can be found in the appendix under A.1.1.

In resonance the free evolution between kicks vanishes and consequently the time evolution of the sytem can be charaterised by just one parameter $K = T \cdot k$ (besides τ and β of course), instead of two. Where k is the kick strength and T is the number of kicks:

$$\hat{U}^T = \left[\exp\left(-ik\cos\left(\hat{\theta}\right) \right) \right]^T = \exp\left(-iTk\cos\left(\hat{\theta}\right) \right) = \exp\left(-iK\cos\left(\hat{\theta}\right) \right) \quad (1.11)$$

Now let us investigate the change in energy the QKR experiences over time, departing from the initial state $|m\rangle$ in momentum space, where m is the momentum quantum number. We will consider the kinetic energy only, because the potential vanishes outside of the δ-kicks.

$$\langle E(K) \rangle = \langle \psi(K) | \hat{E}_{kin} | \psi(K) \rangle = \langle \psi(K) | \frac{\hat{p}^2}{2} | \psi(K) \rangle = \frac{K^2}{4} + \frac{m^2}{2} \qquad (1.12)$$

The result in equation (1.12) means that the energy grows quadratically with K implying that it grows quadratically with the kick strength k and the number of kicks T, full derivation under A.1.2. Additionally the initial energy is given by $\frac{m^2}{2}$ as expected.

In quantum resonance an analytical solution for the time evolution in momentum space has been found. $P(n, t|n_0, \beta)$ is the probability to measure the momentum quantum number n after t evolution steps, departing from a state in n_0 with quasi-momentum β [21]:

$$P(n, t|n_0, \beta) = J_{n-n_0}^2 \left(k \, |W_t| \right) \qquad (1.13)$$

$$W_t = W_t(\xi) = \sum_{s=0}^{t-1} \exp\left(-is\xi \right) \qquad (1.14)$$

$$\xi = \pi l(2\beta \pm 1) \in [0, 2\pi) \qquad (1.15)$$

Here l is an integer defined by the choice $\tau = 2\pi l$ and J_{n-n_0} is the Bessel function of the first kind of the order $n - n_0$.

1.1.3 Quantum Ratchets

Similarly to classical ratchets, quantum ratchets favour a movement or expansion in a certain direction. One of the observables of interest in this thesis will be

the momentum distribution of a wavefunction and its evolution under the Floquet operator, e.g. (1.3). An initial wavefunction favouring positive or negative momenta after its time evolution in resonance (see 1.1.2), is what we refer to as a quantum ratchet. The simplest example being:

$$|\psi(\phi)\rangle = \frac{1}{\sqrt{2}} \left(|n = 0\rangle + e^{-i\phi} |n = 1\rangle \right) \tag{1.16}$$

To show why these states are called ratchet states we will calculate the expectation value of momentum, for the resonant case $\beta = 0$ and $\tau = 4\pi$:

$$\langle p(K, \phi)\rangle = \langle \psi(K, \phi)| \, \hat{p} \, |\psi(K, \phi)\rangle = \frac{1}{2} + \frac{K}{2} \sin(\phi) \tag{1.17}$$

A detailed derivation can be found under A.1.3. The result (1.17) proves, that for $\phi \neq \pi z$ with $z \in \mathbb{Z}$ we have our hands on a quantum ratchet state.

1.1.4   Antiresonance

A QKR can be configured in such a way, that after any even number of kicks the wavefunction returns to its initial form. In other words the time evolution operator for two consecutive kicks is equivalent to unity. This phenomenon is called antiresonance and in this subsection two approaches to describe it will be depicted:

1. transformation of every other Floquet operator $\hat{U}$

2. transformation of the Hamiltonian $\hat{H}$ to a new reference frame

Let us mount the mathematically less demanding transformation first and turn our attention to the successive application of two Floquet operators as derived for a general QKR. We choose $\tau = 4\pi f$ with $f \in \mathbb{N}$

$$\hat{U} \cdot \hat{U} = e^{-i\hat{n}\beta 4\pi f} \exp\left(-ik \cos\left(\hat{\theta}\right)\right) \cdot e^{-i\hat{n}\beta 4\pi f} \exp\left(-ik \cos\left(\hat{\theta}\right)\right) \tag{1.18}$$

We used the result from (1.7) and dropped the factors $e^{-i2\pi f \hat{n}} \equiv \mathbb{1}$ and the global phases $e^{-i\beta^2 2\pi f}$. Since $\hat{n}$ and $\hat{\theta}$ correspond to conjugated observables the factors $e^{-i\hat{n}\beta 4\pi f}$ can be identified as translational operators with regard to θ. A special case arises if:

$$\beta\tau = \pi \quad (\text{mod } 2\pi) \tag{1.19}$$

$$\hat{U} \cdot \hat{U} = e^{-i\hat{n}\pi} \exp\left(-ik \cos\left(\hat{\theta}\right)\right) \cdot e^{-i\hat{n}\pi} \exp\left(-ik \cos\left(\hat{\theta}\right)\right)$$

$$\equiv e^{i\hat{n}\pi} \exp\left(-ik \cos\left(\hat{\theta}\right)\right) e^{-i\hat{n}\pi} \exp\left(-ik \cos\left(\hat{\theta}\right)\right)$$

$$= \hat{T}_\theta^\dagger(\pi) \exp\left(-ik \cos\left(\hat{\theta}\right)\right) \hat{T}_\theta(\pi) \exp\left(-ik \cos\left(\hat{\theta}\right)\right)$$

$$= \exp\left(ik \cos\left(\hat{\theta}\right)\right) \exp\left(-ik \cos\left(\hat{\theta}\right)\right) \equiv \mathbb{1} \tag{1.20}$$

The special case discussed here is obviously that of antiresonance, after any even number of kicks the system returns to its initial wavefunction. All configurations leading to antiresonance are captured in (1.30).

Now for the second approach to antiresonance. To better understand what antiresonance is, we will apply the unitary transformation $\hat{G}$, defined through its generator λ:

$$\lambda = -\beta(\hat{p}t - 2\hat{x}) \tag{1.21}$$

A physical interpretation of $\hat{G}$ can be derived through consideration of the translational operator in position space $e^{-i\hat{p}\beta t}$, shifting the space coordinate by βt, and the translational operator in momentum space $e^{i\hat{x}2\beta}$, shifting the momentum coordinate by -2β. In this sense $\hat{G}$ cancels out $\beta\hat{n}$ in the kinetic energy term of the Schrödinger equation by shifting the reference frame, see (1.32).

$$\hat{G} = e^{i\lambda} = e^{-i\beta(\hat{p}t - 2\hat{x})} \tag{1.22}$$
$$\psi(x,t) \rightarrow \psi'(x,t) = \hat{G}\,\psi(x,t) = e^{-i\beta(\hat{p}t - 2\hat{x})}\psi(x,t) \tag{1.23}$$

Now we have to find the new Schrödinger equation for $\psi'(x,t)$, which is equivalent to our original formulation for $\psi(x,t)$. In the following we will be studying the antiresonant case only.
As a quick reminder we will recapitulate the original Hamiltonian $\hat{H}$:

$$\hat{H}\psi(x,t) = i\partial_t\psi(x,t) \overset{?}{\Longleftrightarrow} \hat{H}'\psi'(x,t) = i\partial_t\psi'(x,t) \tag{1.24}$$
$$\hat{H} = \frac{\hat{p}^2}{2} + k\cos(\hat{x}) \cdot \sum_{n=0}^{\infty} \delta(t - n\tau) \tag{1.25}$$

The new Hamiltonian $\hat{H}'$ satisfying the condition (1.24) is of the following form:

$$\hat{H}' = \frac{1}{2}\left(\hat{p} - \partial_x\lambda\right)^2 - \partial_t\lambda + k\cos(\hat{x}) \cdot \sum_{n=0}^{\infty} (-1)^n\delta(t - n\tau)$$
$$= \frac{(\hat{p} - 2\beta)^2}{2} + \beta\hat{p} + k\cos(\hat{x}) \cdot \sum_{n=0}^{\infty} (-1)^n\delta(t - n\tau) \tag{1.26}$$

At this point the factor $(-1)^n$ added to the kicking potential might seem out of place, but it is necessary as $\hat{G}$ and the kicking potential do not commutate (more on this under A.1.4). In fact this very factor $(-1)^n$ is the reason for destructive interference in the antiresonant case, $\hat{p} - \beta$ suppresses the free evolution and successive kicks cancel out. Later the condition for antiresonance constricting β and τ will emerge due to the factor discussed.

To prove that (1.24) is fulfilled by $\hat{H}'$ we need to verify the following equality, because it is the result of inserting the definition (1.23) into (1.24):

$$\hat{H} - i\partial_t = \hat{G}^\dagger \left[\hat{H}' - i\partial_t \right] \hat{G} \tag{1.27}$$

A step by step solution can be found under A.1.4. Here only a shortened will be presented, importantly we use $\beta\tau = \pi \ (\mathrm{mod}\ 2\pi)$ when commutating $\hat{G}$ and the delta-kicking potential:

$$\hat{G}^\dagger \left[\hat{H}' - i\partial_t \right] \hat{G} = \hat{G}^\dagger \left[\hat{G}\,\frac{\hat{p}^2}{2} + \beta\hat{p}\hat{G} + \hat{G}k\cos(\hat{x}) \cdot \sum_{n=0}^{\infty} \delta(t - n\tau) - \hat{G}i\partial_t - \beta\hat{p}\hat{G} \right]$$

$$= \frac{\hat{p}^2}{2} + k\cos(\hat{x}) \cdot \sum_{n=0}^{\infty} \delta(t - n\tau) - i\partial_t$$

$$= \hat{H} - i\partial_t \tag{1.28}$$

With the transformation completed let us finally get back to the main point of this section, antiresonance. Therefore we choose $\tau = 4\pi f$ with $f \in \mathbb{N}$ and ask ourselves for which values of β will two consecutive kicks negate each other?
The answer to this question emerges during the derivation of (1.28):

$$\beta\tau \stackrel{!}{=} \pi \quad (\mathrm{mod}\ 2\pi) \tag{1.29}$$

$$\beta = \frac{2i + 1}{4f} \qquad\qquad i \in \{0, ..., 2f - 1\} \tag{1.30}$$

An important example for an antiresonant configuration is $\beta = 1/4$ at $\tau = 4\pi$. The derivation of (1.30) is analogous to A.1.1. The check our result we calculate the one cycle Floquet operator for $\hat{H}'$ just as we did in (1.3), except for the new period in time of 2τ instead of just τ.

$$\hat{U}' = e^{ik\cos(\hat{x})} e^{-ik\cos(\hat{x})} \equiv \mathbb{1} \tag{1.31}$$

The factors $e^{-i2\pi fn}$ stemming from the free evolution between kicks have been dropped immediatly, as well as the global phase $e^{-i3\beta^2}$. The first factor is the inverse of the second one, just as expected.
Lastly let us reconsider the transformed Hamiltonian in antiresonance, but rewritten in a different form, using (1.6):

$$\hat{H}' = \frac{\hat{n}^2}{2} + \frac{3\beta^2}{2} + k\cos(\hat{x}) \sum_{n=0}^{\infty} \delta(t - 2n\tau) - k\cos(\hat{x}) \sum_{n=0}^{\infty} \delta(t - (2n+1)\tau) \tag{1.32}$$

Now that we have absorbed the factor $(-1)^n$ it should be clear why the physics described by (1.32) is periodic in time with a period of 2τ. Moreover it seems that a QKR in antiresonance can be interpreted as a double kicked quantum rotor with trivial time evolution.

1.2 Experiment

The experimental implementation this work is largely based around builds on the atomic optics kicked rotor (AOKR for short), which was realized for the first time by the Raizen group [15]. In this thesis however more current setups using Bose-Einstein condensates (BEC) will be discussed [20].

To create the BEC, atoms are held in an magneto-optical trap and cooled down, using laser cooling as well as evaporative cooling. Once the temperature has fallen below the critical point for BEC formation the atoms are released and the actual experiment begins. A standing wave laser generates the kicking potential, with the delta-like behaviour beeing induced through an acousto-optic modulator. The density of the BEC is small enough to neglect interactions between the atoms and at the same time its low temperature allows for sharp momentum peaks to be observed.

After the kicks have been applied, the BEC expands freely (under the effect of gravity only) to allow for time-of-flight imaging. Near resonant light is shined on the BEC, the subsequent flourescence is captured by a CCD-sensor (charge coupled device) to deduce the momentum distribution.

1.2.1 Rescaling

Before rescaling of any sort is applied, the Hamiltonian of an AOKR is given by:

$$\hat{H}_{AOKR} = \frac{\hat{p}^2}{2M} - V_0 \cos\left(2k_L \hat{x}\right) \sum_{n=0}^{\infty} \delta\left(t - \tau n\right) \tag{1.33}$$

In (1.33) M is the mass of an atom, V_0 is the amplitude of the standing wave, k_L is the wavevector of the standing wave and τ is the kicking period. To arrive at the more compact form (1.1) we used in the theory section, the following steps are necessary:

$$E \rightarrow \frac{E}{8\frac{\hbar^2 k_L^2}{2M}} \tag{1.34}$$

$$\hat{p} \rightarrow \frac{\hat{p}}{2\hbar k_L} \tag{1.35}$$

$$\hat{x} \rightarrow 2k_L \hat{x} \tag{1.36}$$

$$\tau \rightarrow 2\pi \frac{\tau}{T_{1/2}} \tag{1.37}$$

When rescaling the kicking period τ in (1.37) we used the Half-Talbot time $T_{1/2}$, which is defined as:

$$T_{1/2} = \frac{2\pi M}{4\hbar k_L^2} \tag{1.38}$$

Since infinitely short delta-kicks are unattainable in the experiment, the kick duration $\triangle T$ has to be addressed in the rescaling process. We define the kicking strength k as:

$$k = \frac{V_0 \, \triangle T}{\hbar} \tag{1.39}$$

Finally we obtain the rescaled Hamiltonian:

$$\hat{H} = \frac{\hat{p}^2}{2} + k \cdot \cos\left(\hat{x}\right) \cdot \sum_{n=0}^{\infty} \delta(t - n\tau) \tag{1.40}$$

Chapter 2

Quantum Walks

A simple classical random walk consists of a walker in one dimension, who randomly (e.g. through a coin flip) chooses to make a step to the left or to the right and repeats this process a specified amount of times (see 2.1a). Therefore classical random walks are a prime example for binomial probability distributions and their convergence to a Gaussian distribution for a large number of steps, as predicted by the law of large numbers. From a quantum mechanical perspective a classical random walk is one where every step is succeeded by a position measurement, leading to the collapse of the wavefunction.

Quantum random walks on the contrary rely on the coherence of the wavefunction during the entire process of the walk, highlighted in figure 2.1b. Measurements are conducted only after all the steps of the walk are completed, because any measurement is a form of decoherence. The idea of quantum random walks was proposed for the first time in 1993 [1] and ever since it has been an important topic of research in the field of quantum information theory, as many quantum search algorithms build on quantum walks [19].

For an in-depth introduction to quantum walks please consult [10], here we will only recapitulate the main definitions required. Firstly the walker has to feature an internal degree of freedom, allowing us apply a translation whose direction is determined by the internal state. Such an internal degree of freedom could be generated by the spin 1/2 states $|\uparrow\rangle$ and $|\downarrow\rangle$ or two hyperfine states $|1\rangle$ and $|2\rangle$. After every translation the system is brought back into a superposition of the two states the internal degree of freedom gives us access to.

(a) classical walk
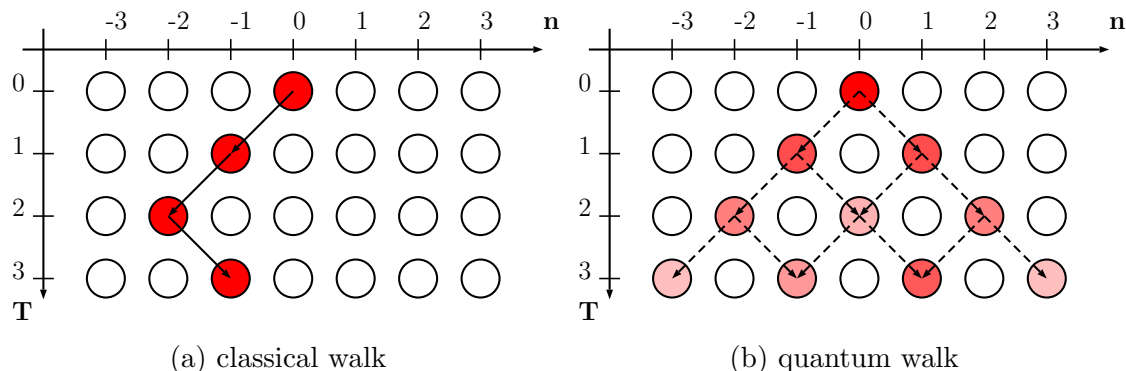
(b) quantum walk

Figure 2.1: Comparing three steps of one-dimensional random walks

The process creating this superposition represents the quantum mechanical analogon to the coin flip encountered in classical random walks and therefore the matrix used to superimpose the two internal states is referred to as the coin matrix. Recreating the superposition is necessary, because with the application of a translation, which depends on the internal state, the superposition is destroyed. In this thesis the following notation will be used:

$$|\uparrow\rangle \equiv |F = 1\rangle \equiv \begin{pmatrix} 1 \\ 0 \end{pmatrix}, \qquad |\downarrow\rangle \equiv |F = 2\rangle \equiv \begin{pmatrix} 0 \\ 1 \end{pmatrix} \tag{2.1}$$

Then possible coin matrices include the two following balanced ones:

$$H = \frac{1}{\sqrt{2}} \begin{pmatrix} 1 & 1 \\ 1 & -1 \end{pmatrix} \tag{2.2}$$

$$Y = \frac{1}{\sqrt{2}} \begin{pmatrix} 1 & i \\ i & 1 \end{pmatrix} \tag{2.3}$$

One iteration of an ideal quantum random walk in one dimension is described by the unitary operator:

$$\hat{U} = \left(\mathbb{1} \otimes \hat{C} \right) \cdot \hat{S} = \left(\mathbb{1} \otimes \hat{C} \right) \cdot \left(|\uparrow\rangle \langle\uparrow| \otimes \sum_i |i+1\rangle \langle i| + |\downarrow\rangle \langle\downarrow| \otimes \sum_i |i-1\rangle \langle i| \right) \tag{2.4}$$

The step operator $\hat{S}$ shifts $|\uparrow\rangle$ states to the right and $|\downarrow\rangle$ states to the left (for example in position space), after that the coin of choice $\hat{C}$ recreates a superposition in the internal state. With the introduction of the general translation operator $\hat{T}$ we can rewrite $\hat{U}$ in a more compact and general form. Here $\hat{T}_x(d)$ represents a shift by d in position space and $\hat{T}_p(d)$ respectively in momentum space:

$$\hat{T}_x(d) = e^{-i\hat{p}d}, \qquad \hat{T}_p(d) = e^{-i\hat{x}d} \tag{2.5}$$

$$\hat{U} = \left(\mathbb{1} \otimes \hat{C} \right) \cdot \exp\left(-i\hat{x}d \otimes 2\hat{S}_z \right) \tag{2.6}$$

The operator $\hat{S}_z$ is defined by its eigenstates in (2.1), its corresponding observable is the spin component in z-direction.

$$\hat{S}_z = \frac{1}{2} \left(|\uparrow\rangle \langle\uparrow| - |\downarrow\rangle \langle\downarrow| \right) \equiv \frac{1}{2} \begin{pmatrix} 1 & 0 \\ 0 & -1 \end{pmatrix} \tag{2.7}$$

Figure 2.2 concludes the discussion of the ideal quantum random walk with a simulation of an ideal walk using the balanced Y coin and a unit stepsize in momentum space. Due to dominant destructive interference on the right, the walk is asymmetric.
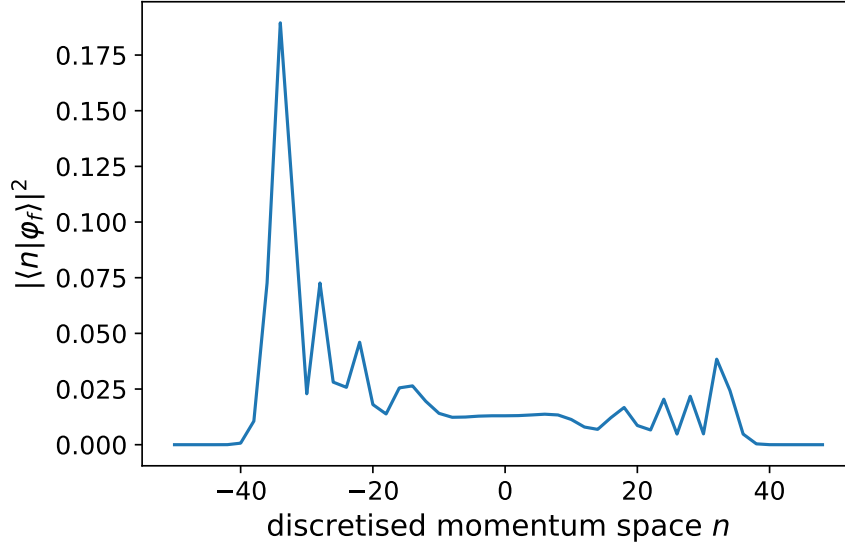
Figure 2.2: Even points of the probability distribution for an ideal quantum walk with Y coin after 50 steps, starting with $\varphi_i = |0\rangle \otimes |\uparrow\rangle$

2.1 QKR Walks

In this section we will explore the idea of a QKR with variable (in terms of magnitude and sign) kickstrength depending on an internal degree of freedom. The objective is of course to propagate a quantum walk in the experimentally accessible framework of the QKR. The definitions introduced previously in this chapter still apply. In the simplest of cases we want to only change the direction of the kick depending on the internal state, this can be achieved through a slight modification of the Hamiltonian:

$$\hat{H} = \frac{\hat{p}^2 \otimes \mathbb{1}}{2} + k \cos\left(\hat{\theta}\right) \otimes 2\hat{S}_z \cdot \sum_{n=0}^{\infty} \delta(t - n\tau) \tag{2.8}$$

$$\hat{U} = \left(\mathbb{1} \otimes \hat{C}\right) \cdot \hat{S} \tag{2.9}$$

Here $\hat{S}$ is more complex than the simple translation operator used beforehand, we have to integrate over one period τ of the Hamiltonian, see (1.3). After every period the coin operator $\hat{C}$ restores the superposition in the internal state.

$$
\begin{aligned}
\hat{S} &= \exp\left(-i\frac{\tau}{2}\hat{p}^2 \otimes \mathbb{1}\right) \cdot \exp\left(-ik \cos\left(\hat{\theta}\right) \otimes 2\hat{S}_z\right) \\
&= \exp\left(-i\frac{\tau}{2}\hat{p}^2 \otimes \mathbb{1}\right) \cdot \sum_{m=0}^{\infty} \frac{1}{m!} \left(-ik \cos\left(\hat{\theta}\right) \otimes 2\hat{S}_z\right)^m \\
&\equiv \exp\left(-i\frac{\tau}{2}\hat{p}^2\right) \cdot \begin{pmatrix} \exp\left(-ik \cos\left(\hat{\theta}\right)\right) & 0 \\ 0 & \exp\left(ik \cos\left(\hat{\theta}\right)\right) \end{pmatrix}
\end{aligned} \tag{2.10}
$$

We see that $|\uparrow\rangle$ states are kicked in the opposite direction of $|\downarrow\rangle$ states, a detailed derivation can be found in the appendix A.2.1. This approach can be generalised

for the application of arbitrary kicking strengths k_1 and k_2, instead of using $2k\hat{S}_z$ to distinguish between the two internal states we use $\hat{K}$:

$$\hat{K} = k_1 \left|\uparrow\right\rangle \left\langle\uparrow\right| + k_2 \left|\downarrow\right\rangle \left\langle\downarrow\right| \equiv \begin{pmatrix} k_1 & 0 \\ 0 & k_2 \end{pmatrix} \tag{2.11}$$

$$\hat{S} = exp\left(-i\frac{\tau}{2}\hat{p}^2\right) \cdot \begin{pmatrix} \exp\left(-ik_1\cos\left(\hat{\theta}\right)\right) & 0 \\ 0 & \exp\left(-ik_2\cos\left(\hat{\theta}\right)\right) \end{pmatrix} \tag{2.12}$$

This generalisation has been experimentally realised by Gil S. Summy[6]. It becomes evident, that equation (2.10) is a special case of equation (2.12), namely for the symmetric configuration $k = k_1 = -k_2$.

2.1.1   Emulate Ideal Quantum Walk

An important component for the realization of quantum walks in the QKR model are quantum ratchet states, introduced in 1.1.3. Here we will focus on the quantum resonant case $\beta = 0$, $\tau = 4\pi$ and a simple initial ratchet state:

$$\psi_{in} = \sqrt{\frac{1}{2}}\left(\left|n = 0\right\rangle + i\left|n = 1\right\rangle\right) \otimes \left|\uparrow\right\rangle \tag{2.13}$$

In order to find the perfect kicking strength $k = k_1 = -k_2$ at which the QKR walk most closely resembles the ideal quantum walk, as seen in 2.2, a numerical simulation is necessary. The parameter k will be tuned so that the position and height of the noticeable peak on the left side match as well as possible.

(a) QKR walk at $k = 1.56$ (b) ideal quantum walk
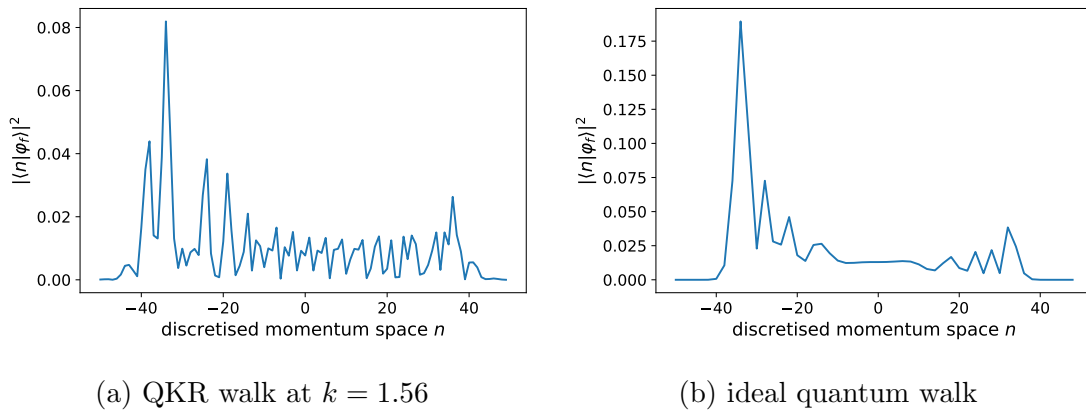
Figure 2.3: probability distribution of QKR and ideal quantum walk after 50 steps

The left peak in 2.3a and in 2.3b are both at $n = -34$, unfortunately the height of the peak could not be reproduced (2.3a shows the best result). Partially explained by the fact that for the ideal walk the probability at uneven points vanishes, while in the QKR walk this is not the case. For the QKR random walk probability density from the peak diffuses to the uneven points and thus the peak is less dominant. To mimic an ideal walk $k = 1.56$ is the optimal choice.

2.1.2 Antiresonance

In section 1.1.4 the phenomenon of antiresonance in the QKR model was introduced, now we want to explore the effect of an antiresonant configuration on QKR walks. In the following subsection the terms resonance and antiresonance always refer to configurations of the pure QKR (without walk). As a reminder for $\tau = 4\pi l$ antiresonance arises for:

$$\beta\tau \overset{!}{=} \pi \quad (\text{mod } 2\pi) \tag{2.14}$$

$$\beta = \frac{2i+1}{4l} \qquad\qquad i \in \{0, ..., 2l-1\} \tag{2.15}$$

Surprisingly the QKR walk does not return to its initial wavefunction after any even number of kicks, as is the case for the pure QKR in antiresonance. Let us compare the time evolution operators representing two kicks for both cases, resonance and antiresonance, in order to draw a connection. Here we use the Y coin as defined in (2.3). The derivation is presented in A.2.2.

$$\hat{W}_{anti} \equiv \frac{1}{2} \begin{pmatrix} 1 - e^{-2ik\cos(\hat{\theta})} & i\left(1 + e^{2ik\cos(\hat{\theta})}\right) \\ i\left(1 + e^{-2ik\cos(\hat{\theta})}\right) & 1 - e^{2ik\cos(\hat{\theta})} \end{pmatrix} \tag{2.16}$$

$$\hat{W}_{res} \equiv \frac{1}{2} \begin{pmatrix} e^{-2ik\cos(\hat{\theta})} - 1 & i\left(1 + e^{2ik\cos(\hat{\theta})}\right) \\ i\left(1 + e^{-2ik\cos(\hat{\theta})}\right) & e^{2ik\cos(\hat{\theta})} - 1 \end{pmatrix} \tag{2.17}$$

Firstly the result in (2.16) proves that for a QKR walk in antiresonant configuration the time evolution is not trivial. Secondly we ask ourselves how the time evolution of a QKR walk in antiresonance differs from that in resonance, to this end we will consider the unitary transformation $\hat{R}$ creating a link between $\hat{W}_{anti}$ and $\hat{W}_{res}$:

$$\hat{R} = \exp\left(i\hat{S}_z\pi\right) \equiv \begin{pmatrix} e^{i\frac{\pi}{2}} & 0 \\ 0 & e^{-i\frac{\pi}{2}} \end{pmatrix} = \begin{pmatrix} i & 0 \\ 0 & -i \end{pmatrix} = i\sigma_z \tag{2.18}$$

The transformation $\hat{R}$ describes a rotation of π around the z-axis in spin-space. If transform $\hat{W}_{anti}$ through $\hat{R}$, we are left with (detailed calculation under A.2.3):

$$\hat{W}'_{anti} = \hat{R}^\dagger \hat{W}_{anti} \hat{R} \equiv \frac{1}{2} \begin{pmatrix} 1 - e^{-2ik\cos(\hat{\theta})} & -i\left(1 + e^{2ik\cos(\hat{\theta})}\right) \\ -i\left(1 + e^{-2ik\cos(\hat{\theta})}\right) & 1 - e^{2ik\cos(\hat{\theta})} \end{pmatrix} \equiv -\hat{W}_{res} \tag{2.19}$$

From (2.19) we conclude that a wavefunction evolves the same way under $\hat{W}_{res}$ and $\hat{W}'_{anti}$, because (-1) can be neglected as a global phase. At this point we can investigate which initial wavefunctions evolve identically in resonance and in antiresonance, as $\hat{R}$ can be applied to the initial wavefunction instead of transforming $\hat{W}$:

$$\psi_{in} \rightarrow \psi'_{in} = \hat{R}\psi_{in} \equiv i\sigma_z\psi_{in} \tag{2.20}$$

If the initial wave function is an eigenvector of σ_z or rather $\hat{S}_z$ it will be unaltered by $\hat{R}$, because applying $\hat{R}$ only introduces an unimportant global phase (given by its eigenvalue of ± 1). Then the time evolution of ψ and ψ' under $\hat{W}_{anti}$ are the same, this means (m is the number of iterations):

$$\left| \langle\psi| \left(\hat{W}^\dagger_{anti}\right)^m \left(\hat{W}_{anti}\right)^m |\psi'\rangle \right|^2 = 1 \tag{2.21}$$

In consequence it will behave identically in resonance and antiresonance, as implied by (2.19). Two simple examples for wavefunctions to which these considerations apply, because they are eigenvectors of σ_z:

$$\psi_1 = \sqrt{\frac{1}{2}} \left(|n=0\rangle + i\,|n=1\rangle\right) \otimes |{\uparrow}\rangle \tag{2.22}$$

$$\psi_2 = \sqrt{\frac{1}{2}} \left(|n=0\rangle + i\,|n=1\rangle\right) \otimes |{\downarrow}\rangle \tag{2.23}$$

To summarize, this technical argument consists of three steps:

1. time evolution through $\hat{W}_{res}$ is equivalent to time evolution through the transformed $\hat{W}'_{anti} = \hat{R}^\dagger \hat{W}_{anti}\hat{R}$, as shown in (2.19)

2. an initial wavefunction, that is an eigenvector of $\hat{R}$, evolves the same way in time under $\hat{W}'_{anti}$ and $\hat{W}_{anti}$

3. combining the first two steps tells us:
   An initial wavefunction, that is an eigenvector of $\hat{R}$, evolves the same way in time under $\hat{W}_{res}$ and under $\hat{W}_{anti}$, therefore in resonance and antiresonance.

But what about initial wavefunctions that are not eigenvectors of σ_z, how do they behave in an antiresonant configuration as compared to a resonant configuration? An important wavefunction of this type is:

$$\psi = \sqrt{\frac{1}{2}} \left(\psi_1 + \psi_2\right) = \sqrt{\frac{1}{2}} |\psi_r\rangle \otimes \left(|{\uparrow}\rangle + |{\downarrow}\rangle\right) \tag{2.24}$$

To improve clarity the ratchet state in momentum space has been labeled as $|\psi_r\rangle$. Due to our coin choice, please refer to (2.3), this wavefunctions time evolution does not change between resonance and antiresonance. The $|{\uparrow}\rangle$-component, ψ_1 in this case, evolves independently of the $|{\downarrow}\rangle$-component ψ_2, because the Y coin will keep one component purely imaginary and one purely real. Mathematically speaking:

$$\left| \langle n| \left(\hat{W}\right)^m |\psi\rangle \right|^2 = \frac{1}{2} \left| \langle n| \left(\hat{W}\right)^m |\psi_1\rangle \right|^2 + \frac{1}{2} \left| \langle n| \left(\hat{W}\right)^m |\psi_2\rangle \right|^2 \tag{2.25}$$

A similar argument is made in [10]. Since we already know that ψ_1 and ψ_2 evolve identically in resonance and in antiresonance, with (2.25) this statement can be extended to ψ as well.

To check this result the momentum distribution with initial wavefunction ψ has been explicitly calculated after two kicks in a resonant and in an antiresonant configuration, please refer to A.2.4

2.2 Experiment

2.2.1 Experimental Difficulties

So far we have worked in the framework of an ideal QKR, of course this situation is experimentally unaccessible. In this subsection three main experimental difficulties, which deviate from an ideal QKR, will be discussed:

1. quasimomentum distribution, β varies across the atoms of the BEC

2. kick-to-kick amplitude fluctuations, k is not constant

3. non-vanishing kick width $d\tau$ (also referred to as $\triangle T$), instead of δ-kicks

Moreover their effect on the momentum distribution will be numerically analysed. All simulations in this subsection will revolve around the following configuration: A resonant QKR walk of twenty steps at a kicking strength $k = 1.56$, using the Y coin from (2.3) and the inital wavefunction $|\psi_{in}\rangle$ from (2.24):

$$|\psi_{in}\rangle = \frac{1}{2}\left(|n = 0\rangle + i\,|n = 1\rangle\right) \otimes \left(|\uparrow\rangle + |\downarrow\rangle\right) \qquad (2.26)$$

The quasimomentum distribution around the resonant $\beta = 0$ is gaussian, because it is impossible (without violating Heisenberg's uncertainty principle) to prepare the BEC in such a way that all atoms have exactly the same momentum. The numerical analysis of the quasimomentum distribution in its effect on the QKR walk builds on the averaging over quantum trajectories, as the interactions between atoms can be neglected we average over single particle simulations. The number of trajectories is of the order 10^3, which corresponds to the number of atoms in the BEC used here [20]. For every trajectory a random quasimomentum β is drawn from the distribution and this β is then conserved during the simulation.

(a) $FWHM = 1\%$ (b) $FWHM = 10\%$
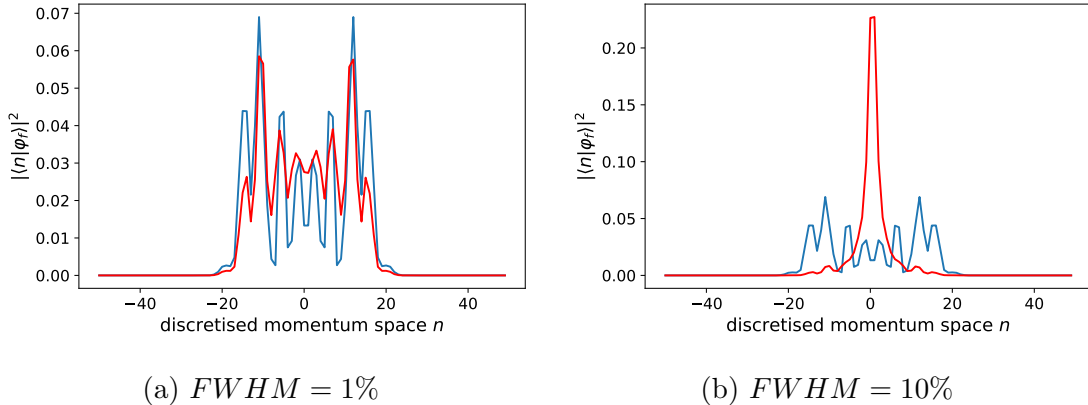
Figure 2.4: Comparison between the ideal case (in blue) and the case where the quasimomentum is described by a normal distribution with the mentioned full width at half maximum (in red), average over 2000 trajectories

At $FWHM = 1\%$ the characteristic spreading of the ideal QKR walk is still present, but the peaks are less sharp as can be seen in 2.4a. In contrast to this the QKR walk collapses completely at $FWHM = 10\%$, since no oscillations and no spreading can be observed in figure 2.4b the quantum features have disappeared. Typically an experimental realization will feature $FWHM \approx 1\%$[20], more on the near resonant quasimomentum distribution [7] and the quantum to classical transition [20].

Secondly we will consider the kick-to-kick fluctuations by drawing a random kicking strength from a normal distribution before every kick. Small vibrations in the optical lattice and fluctuations in the laser amplitude express themselves through varying kick strengths. Again we average over a number of quantum trajectories in the order of 10^3.

(a) $FWHM = k \cdot 15\%$ (b) $FWHM = k \cdot 50\%$
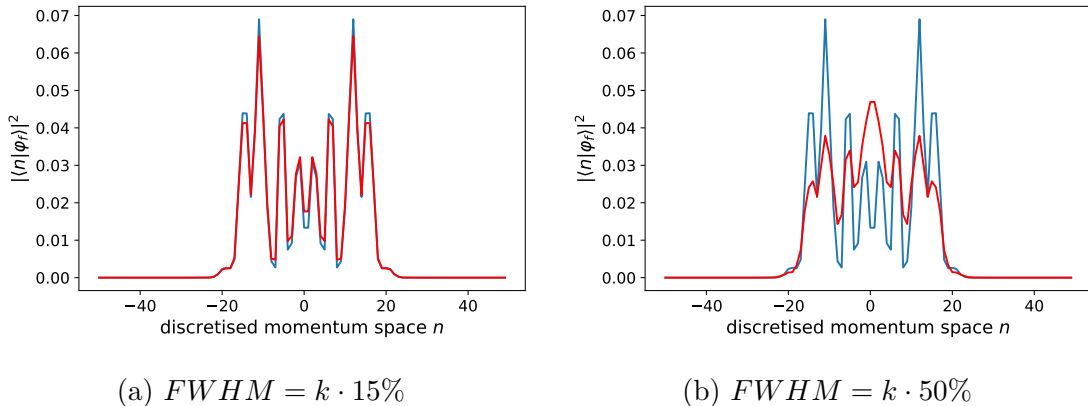
Figure 2.5: Comparison between the ideal case (in blue) and the case where every kickstrength is drawn from a normal distribution with the mentioned full width at half maximum (in red), average over 2000 trajectories

The QKR walk appears to be very robust with regard to varying kick strength, because in experiments $FWHM \leq k \cdot 20\%$ is achievable[17], in fact $FWHM = k \cdot 15\%$ is a typical value. Only at $FWHM = k \cdot 50\%$ do the peaks in the momentum distribution begin to wash out, as seen in figure 2.5b. More details on the effect of

kick-to-kick amplitude fluctuations can be found in [17] and additional results from the simulation can be found in the appendix A.2.5.

The next experimental difficulty to consider is the non-vanishing kick width, obviously infinitely short δ-kicks are impossible to realize. In every experimental implementation the kick has some non-vanishing width in time, referred to in this work as $d\tau$ or $\triangle T$. To simulate this imperfection one δ-kick will be split up into $z \geq 10000$ δ-kicks with strength $k_s = k/z$ and over the interval $d\tau$ these kicks and successively free evolution will be applied, as highlighted in figure 2.7.

(a) ideal δ-kick (b) simulated real kick ($z = 3$)
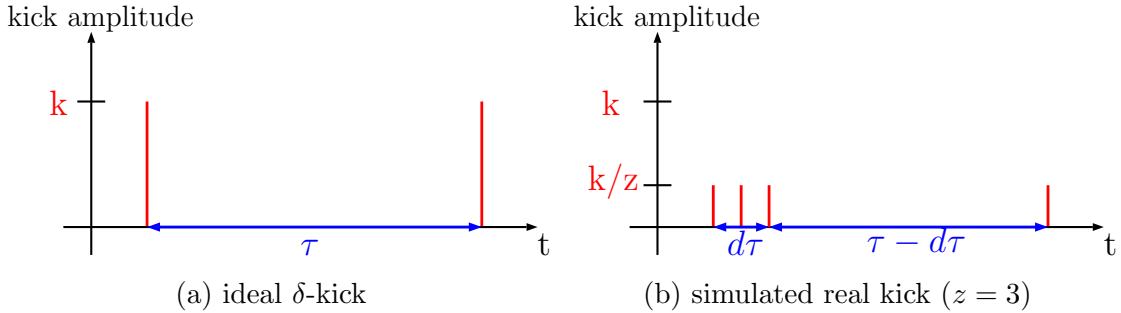
Figure 2.6: Transition from ideal δ-kick to a simulated kick with non-vanishing kick width $d\tau$, through splitting into three δ-kicks

(a) kick width $d\tau = \tau \cdot 1\%$ (b) kick width $d\tau = \tau \cdot 10\%$
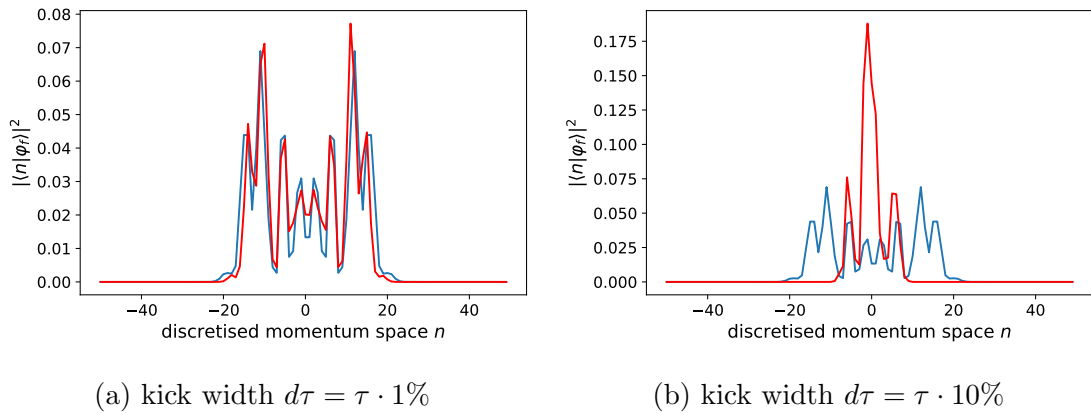
Figure 2.7: Simulations of QKR walks with non-vanishing kick width $d\tau$ with $z = 10000$

In the implementation the parameters are $\tau \approx 100\mu s$ and $d\tau \in [300ns, 1\mu s]$. Consequently kick widths of $d\tau \leq \tau \cdot 1\%$ are technically feasible[7] and the simulation predicts only small deviations in the momentum distribution for those values, see figure 2.7a. Whereas for larger kick widths localization seems to arise, as seen in figure 2.7b.

2.2.2 Experimental Implementation

The experimental setup discussed in this section is an extension of the previously introduced AOKR using a BEC, please consult 1.2 for more information. All we need to add is a mechanism to target the internal hyperfine state, to allow for

the propagation of QKR random walks. In this context the connection to the spin formulation has already been stated in 2.1. The internal hyperfine state is addressed through microwaves (α and χ are tuneable)[20] and the mixing can be described by:

$$
\hat{M}(\alpha, \chi) \equiv \exp\left(-i\frac{\alpha}{2}\left[\sin\left(\chi\right)\sigma_x - \cos\left(\chi\right)\sigma_y\right]\right)
$$
$$
= \begin{pmatrix} \cos\left(\frac{\alpha}{2}\right) & e^{-i\chi}\sin\left(\frac{\alpha}{2}\right) \\ -e^{i\chi}\sin\left(\frac{\alpha}{2}\right) & \cos\left(\frac{\alpha}{2}\right) \end{pmatrix} \tag{2.27}
$$

The operator in equation (2.27) allows for the realization of any coin, this property is proven here A.2.6. Importantly the Y coin used in most of this work is implemented by:

$$
\hat{M}\left(\frac{\pi}{2}, -\frac{\pi}{2}\right) \equiv \sqrt{\frac{1}{2}}\begin{pmatrix} 1 & i \\ i & 1 \end{pmatrix} \tag{2.28}
$$

A notable limitation of the experimental setup is the number of steps that can be coherently realized, the experiment considered in this work is currently capable of a maximum of about twenty steps[7] and therefore the simulations in the previous subsection consisted of twenty steps.

Chapter 3

Background on Topology

What does the term "background on topology" mean?

Topology is a mathematical field, in which basic properties of mathematical objects are studied under the influence of continuous transformations. A simple example to make some sense of these technical terms, is the study of the number of holes (basic property) in three-dimensional bodies (mathematical object). It turns out that all three dimensional bodies with the same number of holes can be transformed into each other without cutting or gluing (continuous transformation), but bodies with different numbers of holes cannot. This is why from a topological point of view a donut and a cup have the same properties, they both have one hole. They consequently share the same topological invariant: $n = 1$, where n is the number of holes.

(a) $n = 1$ (b) $n = 1$ (c) $n = 2$
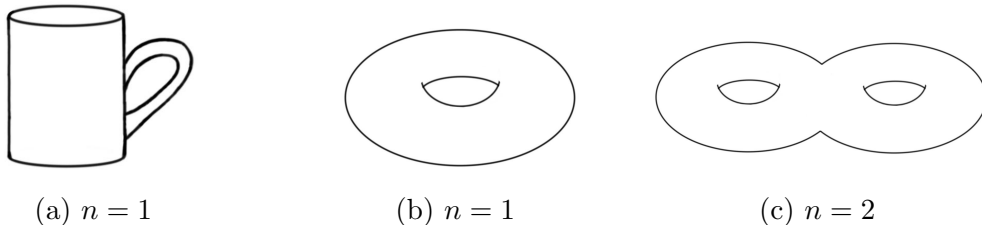
Figure 3.1: three dimensional bodies, classified through the topological invariant n corresponding to the number of holes

Back to physics, here the mathematical objects we study are gapped Hamiltonians and generally their basic property of interest is the number of zero energy eigenstates. Strong statements about gapped Hamiltonians can be made if they are subject to continuous transformations, which additionally do not close the gap, and preserve a symmetrical property (eg. sublattice symmetry). One of these statements is the Bulk-Edge-Correspondence[18], also known as Bulk-Boundary-Correspondence. Moreover in our case, for a periodically driven system, the number of zero and $\pm\pi$ energy eigenstates, reflected by the winding number of the quasienergy spectrum, are topologically protected and therefore resistant to outside noise and perturbations.

3.1   Gapped Hamiltonians

First of all, what is a gapped Hamiltonian?

A gapped Hamiltonian corresponds to a system, where an energy gap separates the first excited state from the zero energy state (or ground state). No energy eigenvalues can be found in a certain region around the zero energy state and this region is called "gap". A simple example for a gapped Hamiltonian can be given by a spin $1/2$ particle in a magnetic field:

$$\hat{H}_{em} = \mu B \hat{S}_y \equiv \mu B \frac{\hbar}{2} \begin{pmatrix} 0 & -i \\ i & 0 \end{pmatrix} = \begin{pmatrix} 0 & H \\ H^\dagger & 0 \end{pmatrix} \qquad (3.1)$$

Adding an electric potential $V \neq |H|$ equates to another gapped Hamiltonian:

$$\hat{H}'_{em} = \mu B \hat{S}_y + \hat{V} \equiv \mu B \frac{\hbar}{2} \begin{pmatrix} V & -i \\ i & V \end{pmatrix} = \begin{pmatrix} V & H \\ H^\dagger & V \end{pmatrix} \qquad (3.2)$$

Now we want to examine the energy spectra (a simple calculation reveals the energy eigenvalues A.3.1) and possible transformations between them. These transformations have to be continuous and their property of interest is the preservation of the energy gap, to allow for topological equivalence[5]. An instructive example is given by the choice $V = 2|H|$, the simplest transformation possible from $\hat{H}_{em}$ to $\hat{H}'_{em}$ is described by:

$$\hat{H}(a) = (1-a) \cdot \hat{H}_{em} + a \cdot \hat{H}'_{em} \qquad\qquad a \in [0,1] \qquad (3.3)$$

This continuous transformation creates a change in the energy spectrum of the system, as highlighted in figure 3.2 where the spectrum is plotted in blue and the zero energy state in red. Clearly it does not conserve the zero energy gap and therefore we cannot use the transformation defined in (3.3) to prove the topological equivalence of the systems described by $\hat{H}_{em}$ and $\hat{H}'_{em}$.
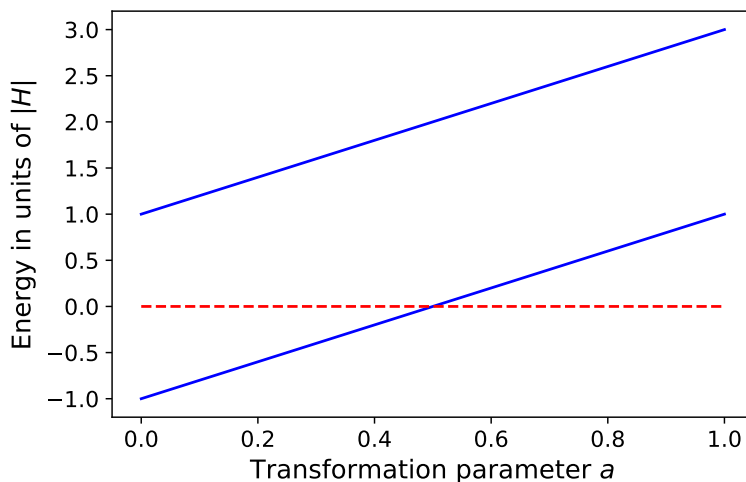
Figure 3.2: Energy spectrum under transformation (3.3) from $\hat{H}_{em}$ to $\hat{H}'_{em}$

At the same time the two gapped Hamiltonians could still be topologically equivalent if there were a continuous transformation that connects them without closing the zero energy gap, so far we checked only one particular transformation. From looking at figure 3.2 however it is evident, that no continuous connection between the two energy spectra is possible without a zero energy crossing. This is a consequence of the intermediate value theorem from basic analysis and a more complex transformation as presented in figure 3.3 cannot make up for this fact.

$$\hat{H}(b) = (1 + b^3 + b - 3b^4) \cdot \hat{H}_{em} + b^2 \cdot \hat{H}'_{em} \qquad b \in [0, 1] \qquad (3.4)$$
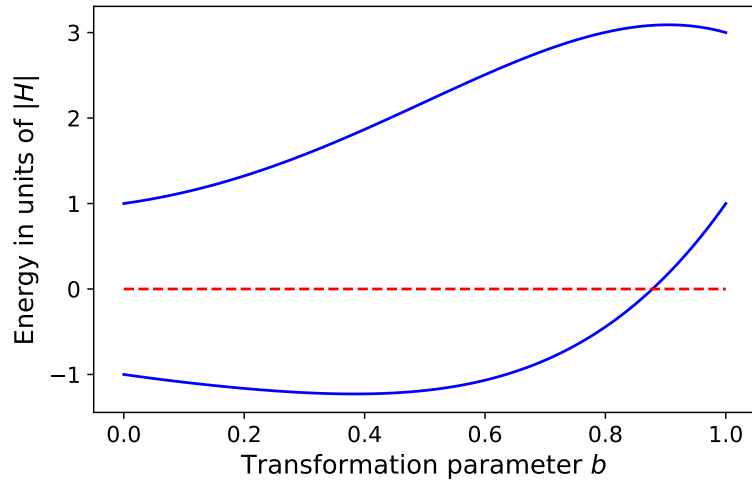
Figure 3.3: Energy spectrum under transformation (3.4) from $\hat{H}_{em}$ to $\hat{H}'_{em}$

In summary the Hamiltonians $\hat{H}_{em}$ and $\hat{H}'_{em}$ are not topologically equivalent, because they can't be continuously transformed into one another without a zero energy crossing that closes the energy gap. Additional reasons why they aren't topologically equivalent will be discussed in the following sections.

3.2 Symmetries

Symmetries play an important role in the topologic classification of a system[16], because they are a requirement for topological invariants. In quantum mechanics symmetries are commonly defined through a unitary operator $\hat{U}_s$ that expresses the symmetry. The symmetry can be tested in the following manner:

$$\hat{U}_s^\dagger \, \hat{H} \, \hat{U}_s \stackrel{?}{=} \hat{H} \qquad (3.5)$$

In the context of topology the more unconventional notion of a "chiral symmetry" proves to be useful[5]:

$$\hat{U}_{cs}^\dagger \, \hat{H} \, \hat{U}_{cs} \stackrel{?}{=} -\hat{H} \qquad (3.6)$$

The chiral symmetry operator $\hat{U}_{cs}$ is often denoted by $\hat{\Gamma}$ in the literature, in this work this notation will be used as well.

3.2.1   Sublattice symmetry

The single most important symmetry that will be referred to in this work is the sublattice symmetry. This chiral symmetry (the terms sublattice symmetry and chiral symmetry are often used synonymously) allows us to break down the description of a lattice into two sublattices, which only interact with each other. In consequence transitions are only possible between points on different sublattices, not between points on the same sublattice. The corresponding symmetry operator $\hat{\Gamma}$ fulfills:

$$\hat{\Gamma}^\dagger \, \hat{H} \, \hat{\Gamma} = -\hat{H} \tag{3.7}$$

Typically $\hat{\Gamma} \equiv \mathbb{1} \otimes \sigma_z$ will be chosen. Important implications can be drawn from equation (3.7)[4], the first one regarding the energy spectrum. Let $|\psi\rangle$ be an eigenstate of the Hamiltonian $\hat{H}$ with energy eigenvalue ϵ:

$$\hat{H} \, |\psi\rangle = \epsilon \, |\psi\rangle \tag{3.8}$$

$$\hat{H} \left(\hat{\Gamma} \, |\psi\rangle \right) = -\hat{\Gamma} \, \hat{H} \, |\psi\rangle = -\epsilon \left(\hat{\Gamma} \, |\psi\rangle \right) \tag{3.9}$$

Since $\hat{\Gamma}$ and $\hat{H}$ do not commute, but instead fulfill (3.8), the expression $\hat{\Gamma} \, |\psi\rangle$ defines a new energy eigenstate with energy eigenvalue $-\epsilon$. Consequently the energy spectrum is symmetric, for every energy eigenstate $|\psi\rangle$ with energy eigenvalue ϵ there exists a different energy eigenstate $\hat{\Gamma} \, |\psi\rangle$ with energy eigenvalue $-\epsilon$. Sublattice symmetry enforces a symmetric energy spectrum.

The following definition is needed to identify the two sublattices a system with sublattice symmetry consists of, the notation from [5] will be used for the sublattice projectors:

$$\hat{P}_A = \frac{1}{2} \left(\mathbb{1} + \hat{\Gamma} \right) \tag{3.10}$$

$$\hat{P}_B = \frac{1}{2} \left(\mathbb{1} - \hat{\Gamma} \right) \tag{3.11}$$

We refer to the sublattices by a subscript A or B respectively. The sublattice projectors work exactly as their names indicate it, a state vector is projected onto its component on the sublattice of choice.

Why are zero energy states special?

If the energy gap were to close and zero energy states would arise, these would feature an interesting property differentiating them from other energy eigenstates. Namely they have to be "localised" to one sublattice exclusively. The reasoning for this goes as follows:

$$\hat{H} \, |\psi_0\rangle = 0 \tag{3.12}$$

$$\Rightarrow \hat{H}\hat{P}_{A/B} \, |\psi_0\rangle = \hat{H}\frac{1}{2} \left(|\psi_0\rangle \pm \hat{\Gamma} \, |\psi_0\rangle \right) = \frac{1}{2} \left(\hat{H} \, |\psi_0\rangle \mp \hat{\Gamma}\hat{H} \, |\psi_0\rangle \right) = 0 \tag{3.13}$$

The equation above implies that, after projecting an arbitrary zero energy eigenstate $|\psi_0\rangle$ to a sublattice either it vanishes or is unchanged, depending on which sublattice we choose. Zero energy states are said to be "their own chiral symmetric partner"[5], this is an equivalent statement. In other words, zero energy eigenstates are eigenstates of the operator $\hat{\Gamma}$ expressing chrial symmetry:

$$\hat{\Gamma}|\psi_0\rangle = \pm|\psi_0\rangle \tag{3.14}$$

Later we will see that zero energy states can arise at the edge of a system with an energy gap.

More types of symmetries and their relation to topological properties are discussed in [2].

3.3 Topological invariants

Why are topological invariants useful?

First we need to restrict the types of transformations that connect topologically equivalent gapped Hamiltonians, this is analogous to the ban on "glueing" and "cutting" in transformations between the objects in figure 3.1. Two important properties we require are continuity (defined in analysis) and the preservation of the energy gap, as stated in the section about gapped Hamiltonians 3.1. Additionally the symmetries of the system, e.g. sublattice symmetry, have to be conserved throughout the transformation. This is one reason why $\hat{H}_{em}$ and $\hat{H}'_{em}$ can't be topologically equivalent (hinted at at the end of section 3.1), they do not share the same symmetries.

In summary the transformations we are interested in satisfy the following properties:

1. continuity as defined in basic analysis

2. conservation of the energy gap

3. conservation of the symmetries

Such transformations are also referred to as adiabatic deformations[5], a connection to the theory of Berry Curvature and Phases can be drawn[3],[5] as suggested by this name.

Two gapped Hamiltonians are topologically equivalent, if there is a way to transform one Hamiltonian into the other without violating any of the three properties stated. While it is hard to test all possible transformations, two gapped Hamiltonians are topologically equivalent if they possess the same topological invariants. Moreover, topological invariants can predict the number of protected edge states, this will be explained in subsection 3.3.2.

3.3.1 Winding number

Finally, the topological invariant, a large part of this thesis is dedicated to, will be introduced: the winding number.

The winding number captures the topological properties of systems that are described by a chiral symmetric Hamiltonian with a discrete translational symmetry (lattice structure) in position or momentum space (said to be in class A III)[16]. Previously when the notion of a gapped Hamiltonian was introduced in 3.1, a flat dispersion relation or rather a zero-dimensional external degree of freedom was implicitly assumed. Most systems however feature a more complex, non-constant dispersion relation, these systems include the one we want to study here. Nevertheless, the dispersion relation has to maintain the energy gap and this property coins the term topological insulator used in the literature[16].

Here we want to focus on Hamiltonians composed of an external degree of freedom (e.g. position in momentum or position space) and an internal degree of freedom (e.g. spin 1/2). In the setting that will be discussed the Hamiltonian is periodic in one-dimensional position space and the energy spectrums dependence on position will be studied. Periodicity in position space equates to a lattice structure in momentum space, implied by Bloch's Theorem.

$$\hat{H}(x) = \hat{H}(x + 2\pi) \tag{3.15}$$

The energy spectrum depends on the one-dimensional position and is therefore periodic, whereas the internal spin 1/2 degree of freedom is the source of the chiral symmetry. We choose to implement the lattice structure in momentum space instead of position space, which would be more common. This choice is relatively unimportant, because it only affects the naming convention and a few signs not the fundamental behaviour of the winding number. In later chapters however it will prove useful. The chiral symmetry operator $\hat{\Gamma}$ allows for the following conclusions:

$$\hat{\Gamma} \equiv \mathbb{1} \otimes \sigma_z \tag{3.16}$$

$$\hat{\Gamma}^\dagger \hat{H} \hat{\Gamma} = -\hat{H} \tag{3.17}$$

$$\Rightarrow \hat{H} = \hat{H}_{ext} \otimes \hat{H}_{int} \equiv \begin{pmatrix} 0 & H(x) \\ H^*(x) & 0 \end{pmatrix} = E(x)\ \vec{n}(x) \cdot \vec{\sigma} \tag{3.18}$$

Here $\vec{\sigma}$ is the Pauli vector, $\vec{n}(x)$ is a normalised vector and $\pm E(x)$ is the symmetric energy spectrum. Equation (3.17) implies that $\hat{H}_{int}$ cannot depend on σ_z and $\mathbb{1}$, from this we deduce equation (3.18) and $\vec{n}(x) = (n_1(x),\ n_2(x),\ 0)$. The energy spectrum is gapped around zero energy, $\vec{n}(x)$ is confined to a plane and periodic as $E(x)\ \vec{n}(x) = E(x + 2\pi)\ \vec{n}(x + 2\pi)$. Consequently, we can now define the winding number of $E(x)\ \vec{n}(x)$ around the origin of the plane in the positive mathematical sense of rotation.

Looking at figure 3.4 it becomes clear, that the winding number is invariant under continuous transformations respecting the gap around zero energy and chiral symmetry. Violating the energy gap would enable us to "pull" the closed energy curve across the origin, changing the winding number. Whereas violating the chiral symmetry would allow us to "lift" the closed energy curve up from the plane, move it over the origin and "lower" it back into the plane, effectively changing the winding number as well. As the winding number cannot change under adiabatic deformations it is a well-defined topological invariant.
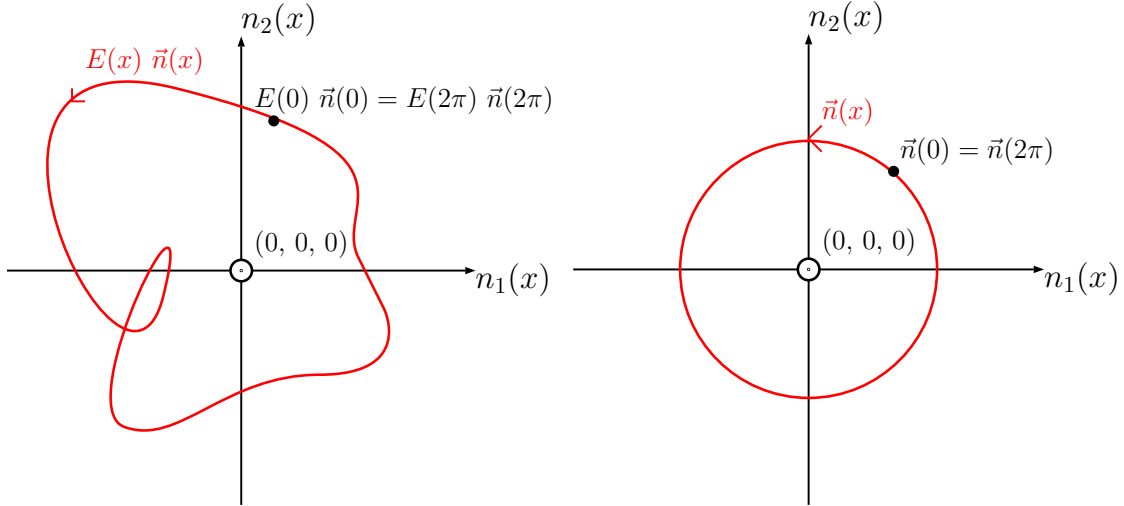
(a) exemplary energy spectrum winding around the origin

(b) $\vec{n}(x)$ contains all the information about the winding number

Figure 3.4: Exemplary energy spectrum with winding number $\nu = 1$

The information about the winding number is completely contained in $\vec{n}(x)$ and to calculate the winding number the following integral needs to be solved:

$$\nu = \int_0^{2\pi} \frac{dx}{2\pi} \left(\vec{n} \times \frac{\partial \vec{n}(x)}{\partial x} \right)_3 \tag{3.19}$$

The "3" in the index stands for the 3-component of the vector inside the brackets. To expose the inner workings of the integral let's visualise the cross product.
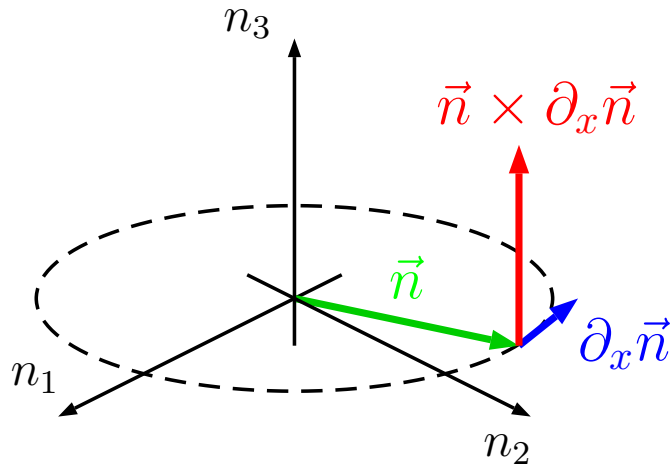
Figure 3.5: Cross product in the winding number integral

The vector $\vec{n}(x)$ is restricted to the $n_1 n_2$-plane and it is normalised, therefore $\partial_x \vec{n}(x)$ is restricted to the same plane and orthogonal to $\vec{n}(x)$. These facts implicate that $\vec{n} \times \partial_x \vec{n}(x)$ has to be perpendicular to the $n_1 n_2$-plane, its only non-vanishing component is the 3-component. The value of its 3-component can be positive or negative and determines the infitesimal circular segment $\vec{n}(x)$ travelled along the unit circle

(dotted line in figure 3.5) due to an infinitesimal change in x.

If we integrate over the 3-component of the cross product and divide by the circumference of the unit circle we are left with equation (3.19) and the winding number we were looking for.

3.3.2   Bulk Edge Correspondence

What is the bulk?

The bulk denotes the portion of system possessing translational symmetry or rather periodicity in the external degree of freedom. In the case of a one-dimensional lattice structure, the bulk is the large central part where edge effects can be neglected. So far, we have treated the bulk Hamiltonian, topological invariants are properties of the bulk.

What is the edge?

At the edge, sometimes also referred to as boundary, translational symmetry in the external degree of freedom no longer holds. For a one-dimensional chain the literal edge corresponds to this topological term, but often there is no clear-cut transition from the edge to the bulk. Since symmetries are broken at the edge, a Hamiltonian different from the bulk Hamiltonian governs their behaviour and interesting protected states can form (e.g. zero energy states).

How do the bulk and the edge influence each other?

Based on its symmetries a gapped bulk Hamiltonian can be topologically classified[16], revealing its topological invariant (e.g. the winding number). Due to the bulk edge correspondence the topological invariant of the bulk equates to the number of protected zero energy edge states[18]. This astounding property is a core result of combining topology and physics, it is one of the main reasons for the vast interest in topological insulators. Instead of presenting the extremely complex proof from K-theory, the bulk edge correspondence will be demonstrated through an instructive and popular example: the SSH-chain[8].
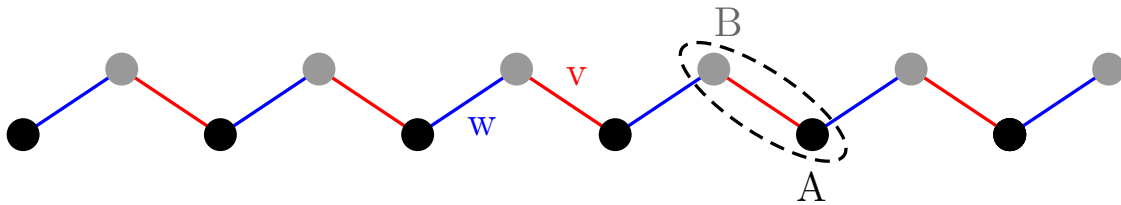
Figure 3.6: SSH chain model, every lattice site (external degree of freedom) is split (dotted line) into two sublattice sites (internal degree of freedom) on the sublattices **A** (black dots) and **B** (grey dots). Transitions inside a lattice cell obey the coupling strength **v**, whereas transition in-between lattice cell obey the coupling **w**.

Clearly the SSH-chain posses sublattice symmetry, because sites on one sublattice couple exclusively with sites on the other sublattice. For $v \neq w$ the Hamiltonian

is gapped, more details in [5]. The appropriate topological invariant is the winding number.

Now we want to consider two limiting cases, $v = 1$ at $w = 0$ and $v = 0$ at $w = 1$. In the case where $v = 1$ at $w = 0$ the winding number of the bulk is $\nu = 1$, whereas for $v = 0$ at $w = 1$ the winding number of the bulk is $\nu = 0$[5]. Thanks to the bulk edge correspondence we can conclude that in the first case, one protected zero energy state per edge should arise. The second case shouldn't feature any protected edge states. Let's visualise the setups mentioned:
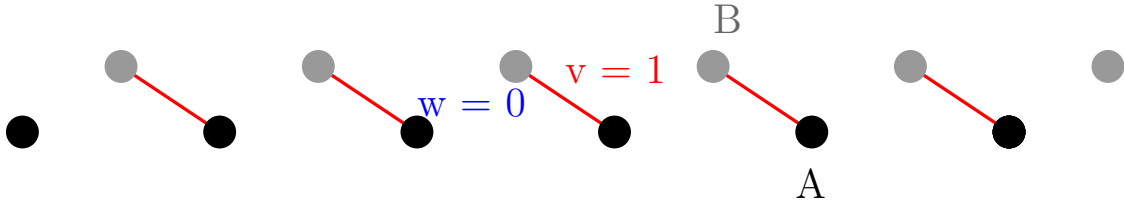
Figure 3.7: Limiting case SSH chain with v = 1 at w = 0, winding number $\nu = 1$

Figure 3.7 shows the topologically interesting case, where a protected zero energy state forms at both edges. As discussed in subsection 3.2.1 the zero energy states are "localised" to one sublattice. Their number per edge corresponds to the winding number of the bulk, highlighting the bulk edge correspondence.
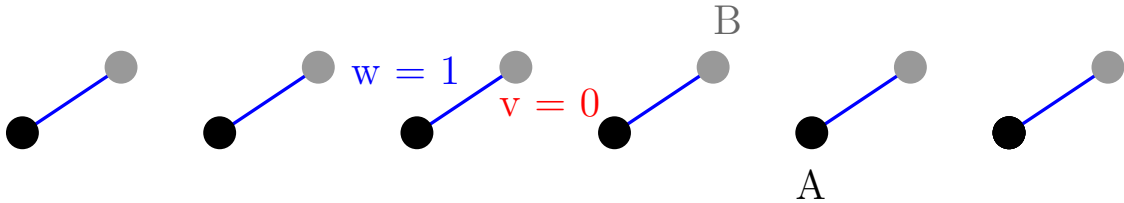
Figure 3.8: Limiting case SSH chain with v = 0 at w = 1, winding number $\nu = 0$

Contrary to the previous limiting case, the situation in figure 3.8 is topologically trivial, because no edge states form. The vanishing bulk winding number predicts this behaviour.

Why are the edge states protected?

The bulk edge correspondence draws a connection between the topological invariant of the bulk and the number of edge states. Since the topological invariant cannot change under adiabatic deformations the same must apply for the number of edge states, as it is equal to the topological invariant.

3.4 Periodically Driven Systems

Up to this point we discussed time-independent Hamiltonians, but ultimately we want to get back to quantum walks and their time-dependent Hamiltonians. For a periodically driven system the operator to be topologically analysed is the so-called effective Hamiltonian $\hat{H}_{eff}$, defined as follows:

$$\hat{U} = \exp\left(-i\hat{H}_{eff}T\right) \tag{3.20}$$

Due to rescaling $\hbar$ drops out. $\hat{U}$ denotes the one-cycle Floquet operator of the system (for example a double kicked quantum rotor), it represents one step of period T in the time evolution. The factor T can be absorbed as well if we rescale in units of T, which we will do in the following. Now instead of dealing with the energy spectrum of a time-independent Hamiltonian our attention shifts to the quasienergy spectrum of the effective, time-independent Hamiltonian.

What is quasienergy?

Introducing a time dependence to the Hamiltonian generally adds to the complexity of a system, aspects like its time evolution become harder to calculate, but here we want to consider a special type of time-dependent Hamiltonians. Namely those that are periodic in time and consequently connections to spatial periodicity, Bloch's theorem and quasimomentum can be drawn. In fact the Bloch theorem is a special case of the Floquet theorem, which applies here[9]. The unitary Floquet operator can be decomposed into its eigenstates $|n\rangle$ with knowledge of their eigenvalues $e^{-i\epsilon_n}$ on the unit circle:

$$\hat{U} = \sum_n e^{-i\epsilon_n} |n\rangle \langle n| \tag{3.21}$$

This equation shows why $\epsilon_n \in (-\pi, \pi]$, the eigenvalues ϵ_n of $\hat{H}_{eff}$ also referred to as quasienergies are restricted to an "energy Brillouin zone" in an analogous manner to quasimomentum. Previously the energy spectrum was periodic and unrestricted, for periodically driven systems the additional restriction to values in $(-\pi, \pi]$ can be visualised through a transition from a cylinder to a torus.

(a) Energy spectrum of a time-independent system mapped to a cylinder

(b) Energy spectrum of a periodically driven system mapped to a torus
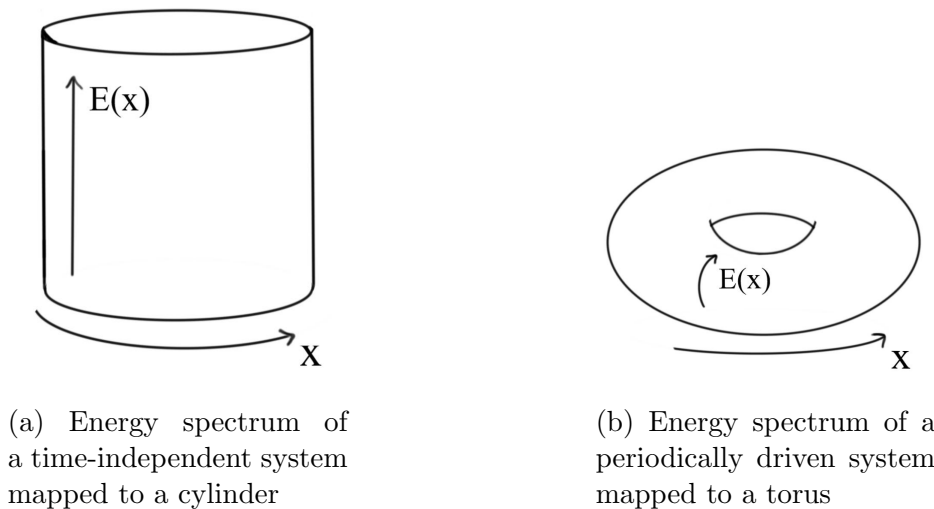
Figure 3.9: Both energy spectra are periodic in x, but for the effective Hamiltonian of a periodically driven system the quasienergy values ϵ_n are only well-defined in the interval $(-\pi, \pi]$, values from outside this interval can be projected onto it by adding or subtracting multiples of 2π

The restriction to quasienergy values in the interval $(-\pi, \pi]$ enables the realisation of new protected edge states, now π energy edge states are possible in addition to zero energy edge states. As discussed in subsection 3.2.1 zero energy eigenstates are special because they are their own chiral symmetric partners, the same applies for π-energy eigenstates in the framework of quasienergy:

$$\hat{H} |\psi_\pi\rangle = \pi |\psi_\pi\rangle \tag{3.22}$$

$$\Rightarrow \hat{H}\hat{\Gamma} |\psi_\pi\rangle = -\pi\hat{\Gamma} |\psi_\pi\rangle \equiv \pi\hat{\Gamma} |\psi_\pi\rangle \tag{3.23}$$

At the edges of a periodically driven system protected zero and π-energy states can form[4]!

Finally, it should be noted that the quasienergy spectrum is unaffected by the choice of the starting point or rather time frame for the Floquet operator, because the Floquet operators for different starting points can be transformed into each other through unitary transformations that leave the eigenstates $|n\rangle$ unaffected.

The choice of timeframe is not trivial at all, because not every timeframe will feature a chiral symmetric Floquet operator. For discrete time quantum walks the most basic restriction a chiral symmetric Floquet operator has to fulfill is "inversion symmetry"[4]. This property describes the invariance of a chiral symmetric Floquet operator $\hat{U}_{cs}$ under time reversal and it implies that $\hat{U}_{cs}$ can be factorised into operators $\hat{A} = \exp(\hat{H}'_1)$ and $\hat{B} = \exp(\hat{H}'_2)$:

$$\hat{U}_{cs} = \hat{A}\hat{B}\hat{A} \tag{3.24}$$

$$\hat{U}_{cs}^\dagger = \left(\hat{A}\hat{B}\hat{A}\right)^\dagger = \hat{A}^\dagger\hat{B}^\dagger\hat{A}^\dagger \tag{3.25}$$

$$\hat{\Gamma}^\dagger\hat{U}_{cs}\hat{\Gamma} = \hat{\Gamma}^\dagger\hat{A}\hat{B}\hat{A}\hat{\Gamma} = \hat{A}^\dagger\hat{B}^\dagger\hat{A}^\dagger = \hat{U}_{cs}^\dagger \tag{3.26}$$

The last equation holds if $\hat{A}$ and $\hat{B}$ are chiral symmetric. The reasoning for the importance of inverion symmetry can be clarified by considering a Floquet operator $\hat{U}'$ that can only be factorised using three different chiral symmetric operators $\hat{A} = \exp(\hat{H}'_1)$, $\hat{B} = \exp(\hat{H}'_2)$ and $\hat{C} = \exp(\hat{H}'_3)$:

$$\hat{U}' = \hat{A}\hat{B}\hat{C} \tag{3.27}$$

$$\hat{U}'^\dagger = \left(\hat{A}\hat{B}\hat{C}\right)^\dagger = \hat{C}^\dagger\hat{B}^\dagger\hat{A}^\dagger \tag{3.28}$$

$$\hat{\Gamma}^\dagger\hat{U}'\hat{\Gamma} = \hat{\Gamma}^\dagger\hat{A}\hat{B}\hat{C}\hat{\Gamma} = \hat{A}^\dagger\hat{B}^\dagger\hat{C}^\dagger \neq \hat{U}'^\dagger \tag{3.29}$$

Again the last equation holds if $\hat{A}$, $\hat{B}$ and $\hat{C}$ are chiral symmetric, but the Floquet operator $\hat{U}'$ cannot be chiral symmetric if $\hat{A} \neq \hat{C}$. Meaning that inversion symmetry is required for chiral symmetry to arise.

Chapter 4

Double Kicked Quantum Rotor

Why are double kicked quantum rotors topologically interesting?

The next objective is to apply the theory on topology from the previous chapter to kicked rotor systems, possibly in combination with quantum walks. A naive approach to this would be to consider the simple model from (2.8), with the slight modification of replacing $\hat{S}_z$ with $\hat{S}_x$ to reveal the necessary chiral symmetry.

$$\hat{H} = \frac{\hat{p}^2 \otimes \mathbb{1}}{2} + k\cos\left(\hat{\theta}\right) \otimes 2\hat{S}_x \cdot \sum_{n=0}^{\infty} \delta(t - n\tau) \tag{4.1}$$

$$\hat{U} = \left(\mathbb{1} \otimes \hat{Y}\right) \cdot \hat{S} \equiv \frac{1}{\sqrt{2}} \begin{pmatrix} \cos\left(\kappa\right) + \sin\left(\kappa\right) & i\cos\left(\kappa\right) - i\sin\left(\kappa\right) \\ i\cos\left(\kappa\right) - i\sin\left(\kappa\right) & \cos\left(\kappa\right) + \sin\left(\kappa\right) \end{pmatrix} \tag{4.2}$$

A short derivation of $\hat{U}$ can be found in the appendix A.4.1, here $\kappa = k\cos(\theta)$ improves clarity. To check chiral symmetry we apply the chiral symmetry operator $\hat{\Gamma} \equiv \mathbb{1} \otimes \sigma_z$, details under A.4.1:

$$\hat{\Gamma}^\dagger \hat{U} \hat{\Gamma} = \hat{\Gamma} \hat{U} \hat{\Gamma} = \hat{U}^\dagger \tag{4.3}$$

This is equivalent to $\hat{\Gamma}^\dagger \hat{H}_{eff} \hat{\Gamma} = -\hat{H}_{eff}$, because the portion of $\hat{H}_{eff}$ that acts on the internal degree is real valued and $\hat{U} = e^{-i\hat{H}_{eff}}$. Therefore equation (4.3) represents an alternative definition of chiral symmetry in periodically driven systems.
As discussed in the previous chapter, the topological properties of this system are described by its topological invariant, the winding number. We can rewrite $\hat{U}$ to get a better glimpse at the winding number:

$$\begin{aligned} \hat{U} &\equiv \frac{1}{\sqrt{2}} \begin{pmatrix} \cos\left(\kappa\right) + \sin\left(\kappa\right) & i\cos\left(\kappa\right) - i\sin\left(\kappa\right) \\ i\cos\left(\kappa\right) - i\sin\left(\kappa\right) & \cos\left(\kappa\right) + \sin\left(\kappa\right) \end{pmatrix} \\ &= \begin{pmatrix} \cos\left(\kappa - \frac{\pi}{4}\right) & -i\sin\left(\kappa - \frac{\pi}{4}\right) \\ -i\sin\left(\kappa - \frac{\pi}{4}\right) & \cos\left(\kappa - \frac{\pi}{4}\right) \end{pmatrix} \\ &= \exp\left(-i\left(\kappa - \frac{\pi}{4}\right)(1,0,0) \cdot \vec{\sigma}\right) \end{aligned} \tag{4.4}$$

Equation (4.4) tells us $\vec{n} = (1,0,0) = const.$ and from equation (3.19) we conclude, that $\nu = 0$. The vanishing winding number indicates a topologically trivial system

and therefore the naiv approach described is uninteresting from a topological point of view.

Nevertheless it is possible to implement topologically non-trivial systems through the use of one-dimensional quantum walks. One possibility is to use a coin creating a position dependent superposition of internal states, this setup is proposed in [4] and [11]:

$$
\begin{aligned}
\hat{C}\left(\hat{x}\right) &\equiv \exp\left(-i\frac{\alpha(x)}{2}\left[\sin\left(\chi(x)\right)\sigma_x - \cos\left(\chi(x)\right)\sigma_y\right]\right) \\
&= \begin{pmatrix} \cos\left(\frac{1}{2}\alpha(x)\right) & e^{-i\chi(x)}\sin\left(\frac{1}{2}\alpha(x)\right) \\ -e^{i\chi(x)}\sin\left(\frac{1}{2}\alpha(x)\right) & \cos\left(\frac{1}{2}\alpha(x)\right) \end{pmatrix}
\end{aligned} \tag{4.5}
$$

In this work however we will focus on a different proposal, building on a double kicked quantum rotor as introduced in [22], it allows for the realisation of topologically non-trivial phases too.

4.1 Theory

The concrete setup of the double kicked quantum rotor with an internal spin-1/2 degree of freedom we will treat here, is given by its Hamiltonian:

$$
\hat{H} = \frac{\hat{p}^2 \otimes \mathbb{1}}{2} + k_1\cos\left(\hat{\theta}\right)\otimes 2\hat{S}_x \cdot \sum_{n=0}^{\infty}\delta(t-2n\tau) + k_2\sin\left(\hat{\theta}\right)\otimes 2\hat{S}_y \cdot \sum_{n=0}^{\infty}\delta(t-(2n+1)\tau) \tag{4.6}
$$

The Floquet operator can now be derived:

$$
\begin{aligned}
\hat{U}_{res} &\equiv e^{-i\frac{\tau}{2}\hat{p}^2}e^{-ik_2\sin\left(\hat{\theta}\right)\sigma_y}e^{-i\frac{\tau}{2}\hat{p}^2}e^{-ik_1\cos\left(\hat{\theta}\right)\sigma_x} \\
&= e^{-iK_2\left(\hat{\theta}\right)\sigma_y}e^{-iK_1\left(\hat{\theta}\right)\sigma_x}
\end{aligned} \tag{4.7}
$$

Where we chose a resonant configuration (free evolution vanishes) and defined $K_1(\hat{\theta}) = k_1\cos(\hat{\theta})$ as well as $K_2(\hat{\theta}) = k_2\sin(\hat{\theta})$ (notation from [22]).

Next up we need to check the important ingredients for the topological analysis of the system, these are chiral symmetry and a gapped quasienergy spectrum. Firstly, chiral symmetry cannot be identified as easily as in previous examples. Instead we have to use the notion of time frames[4] corresponding to different starting points of the Floquet operator.

4.1.1 Chiral sublattice symmetry

For the system presented here two chiral symmetric time frames exist and their Floquet operators are:

$$
\hat{U}_1 = e^{-i\frac{1}{2}K_1\left(\hat{\theta}\right)\sigma_x}e^{-iK_2\left(\hat{\theta}\right)\sigma_y}e^{-i\frac{1}{2}K_1\left(\hat{\theta}\right)\sigma_x} \tag{4.8}
$$

$$
\hat{U}_2 = e^{-i\frac{1}{2}K_2\left(\hat{\theta}\right)\sigma_y}e^{-iK_1\left(\hat{\theta}\right)\sigma_x}e^{-i\frac{1}{2}K_2\left(\hat{\theta}\right)\sigma_y} \tag{4.9}
$$
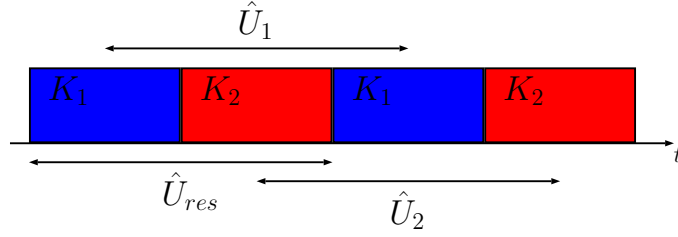
Figure 4.1: Corresponding time frames for the different Floquet operators $\hat{U}_{res}$, $\hat{U}_1$ and $\hat{U}_2$, note that K_1 and K_2 are δ-kicks enlarged here to visualise their amplitude

Both $\hat{U}_1$ and $\hat{U}_2$ are chiral symmetric with regards to $\hat{\Gamma} \equiv \mathbb{1} \otimes \sigma_z$.

$$\hat{\Gamma}^\dagger \hat{U}_1 \hat{\Gamma} = \hat{U}_1^\dagger \tag{4.10}$$

$$\hat{\Gamma}^\dagger \hat{U}_2 \hat{\Gamma} = \hat{U}_2^\dagger \tag{4.11}$$

A detailed proof together with the explicit matrix formulation of $\hat{U}_1$ and $\hat{U}_2$ can be found in the appendix A.4.2.

Are more chiral symmetric variations of the Floquet operator possible?

At this point we want to make sure that our understanding of the chiral symmetry involved is complete and that there are no additional chiral symmetric reformulations (apart from $\hat{U}_1$ and $\hat{U}_2$) of the Floquet operator in (4.7). In order to prove this statement, it suffices to prove the necessity of "inversion symmetry"[4] for the formation of chiral symmetry in this system. The term "inversion symmetry" describes the property $\hat{U}_{is} = \hat{A}\hat{B}\hat{A}$, any variation of the Floquet operator that cannot be rewritten in this fashion cannot have chiral symmetry. An arbitrary Floquet operator for equation (4.6) can be written in one of the following forms:

$$\hat{U} = e^{-i\alpha_1 K_1(\hat{\theta})\sigma_x} e^{-iK_2(\hat{\theta})\sigma_y} e^{-i\alpha_2 K_1(\hat{\theta})\sigma_x} \tag{4.12}$$

$$\hat{U}' = e^{-i\alpha_1 K_2(\hat{\theta})\sigma_y} e^{-iK_1(\hat{\theta})\sigma_x} e^{-i\alpha_2 K_2(\hat{\theta})\sigma_y} \tag{4.13}$$

$$\tag{4.14}$$

Where $\alpha_1, \alpha_2 \in [0,1]$ and $\alpha_1 + \alpha_2 = 1$, because the Floquet operator describes exactly one period T. Applying the unitary transformation $\hat{\Gamma}$, corresponding to chiral symmetry, leaves us with:

$$\hat{\Gamma}^\dagger \hat{U} \hat{\Gamma} = e^{i\alpha_1 K_1(\hat{\theta})\sigma_x} e^{iK_2(\hat{\theta})\sigma_y} e^{i\alpha_2 K_1(\hat{\theta})\sigma_x} \tag{4.15}$$

$$\hat{\Gamma}^\dagger \hat{U}' \hat{\Gamma} = e^{i\alpha_1 K_2(\hat{\theta})\sigma_y} e^{iK_1(\hat{\theta})\sigma_x} e^{i\alpha_2 K_2(\hat{\theta})\sigma_y} \tag{4.16}$$

A detailed calculation can be found in the appendix A.4.2, where the chiral symmetry of $\hat{U}_1$ and $\hat{U}_2$ is proven. The Hermitian conjugate of the arbitrary Floquet operators are:

$$\hat{U}^\dagger = e^{i\alpha_2 K_1(\hat{\theta})\sigma_x} e^{iK_2(\hat{\theta})\sigma_y} e^{i\alpha_1 K_1(\hat{\theta})\sigma_x} \tag{4.17}$$

$$\hat{U}'^\dagger = e^{i\alpha_2 K_2(\hat{\theta})\sigma_y} e^{iK_1(\hat{\theta})\sigma_x} e^{i\alpha_1 K_2(\hat{\theta})\sigma_y} \tag{4.18}$$

Note the important mathematical detail, which highlights the importance of "inversion symmetry":

$$\left(\hat{A}\hat{B}\hat{C}\right)^{\dagger} = \hat{C}^{\dagger}\left(\hat{A}\hat{B}\right)^{\dagger} = \hat{C}^{\dagger}\hat{B}^{\dagger}\hat{A}^{\dagger} \neq \hat{A}^{\dagger}\hat{B}^{\dagger}\hat{C}^{\dagger} \tag{4.19}$$

Since we are looking for chiral symmetric versions of the Floquet operator, equation (4.3) leads us to the conclusion:

$$\hat{\Gamma}^{\dagger}\hat{U}\hat{\Gamma} \stackrel{!}{=} \hat{U}^{\dagger} \tag{4.20}$$

$$\hat{\Gamma}^{\dagger}\hat{U}'\hat{\Gamma} \stackrel{!}{=} \hat{U}'^{\dagger} \tag{4.21}$$

This constraint is satisfied if and only if $\alpha_1 = \alpha_2 = \frac{1}{2}$ (in other words $\hat{C} = \hat{A}$), making $\hat{U}$ and $\hat{U}'$ "inversion symmetric". Moreover we can identify $\hat{U} = \hat{U}_1$ and $\hat{U}' = \hat{U}_2$ for $\alpha_1 = \alpha_2 = \frac{1}{2}$.

From looking at figure 4.1 it is evident that only two formulations of the Floquet operator with "inversion symmetry" are possible, these are $\hat{U}_1$ and $\hat{U}_2$. Therefore no additional chiral symmetric variations of the Floquet operator exist.

Why can we work with $\hat{U}_1$ and $\hat{U}_2$ instead of $\hat{U}_{res}$?

As hinted at in section 3.4 the quasienergy spectrum is independent of the chosen time frame, however this fact is so important that a quick recap is reasonable. We will discuss $\hat{U}_1$ only, because the situation for $\hat{U}_2$ is completely analogous.

$$
\begin{aligned}
\hat{U}_1 &= e^{i\frac{1}{2}K_1(\hat{\theta})\sigma_x} \, \hat{U}_{res} \, e^{-i\frac{1}{2}K_1(\hat{\theta})\sigma_x} \\
&= e^{i\frac{1}{2}K_1(\theta)\sigma_x} \left[\sum_{\theta} e^{-iE(\theta)\vec{n}(\theta)\cdot\vec{\sigma}} \left|\theta\right\rangle\left\langle\theta\right| \right] e^{-i\frac{1}{2}K_1(\theta)\sigma_x} \\
&= \sum_{\theta} e^{-iE(\theta)\vec{n}'(\theta)\cdot\vec{\sigma}} \left|\theta\right\rangle\left\langle\theta\right|
\end{aligned}
\tag{4.22}
$$

The unitary transformation connecting $\hat{U}_{res}$ and $\hat{U}_1$ (or rather $\hat{U}_2$) is a rotation in spin space around the x-axis as a function of θ (or y-axis in the case of $\hat{U}_2$), consequently it leaves the projector $\left|\theta\right\rangle\left\langle\theta\right|$ as well as the quasienergy spectrum $E(\theta)$ unaffected. The transformation acts on the internal degree of freedom only, note the transition from $\vec{n}(\theta)$ to $\vec{n}'(\theta)$. To summarize, we can work with $\hat{U}_1$ and $\hat{U}_2$ to analyse the topological properties of the quasienergy spectrum, because all Floquet operators share the same quasienergy spectrum independently of their respective time frames.

4.1.2 Bulk energy spectrum

To derive the quasienergy spectrum all we need to do is to rewrite the chiral symmetric Floquet operators in the following manner:

$$\hat{U}_l = \sum_{\theta} e^{-iE(\theta)\vec{n}_l \cdot \vec{\sigma}} \tag{4.23}$$

Using the matrix representation of $\hat{U}_1$ and $\hat{U}_2$, derived in the appendix A.4.2 and the identity:

$$e^{-i\varphi\vec{n}\cdot\vec{\sigma}} = \cos\left(\varphi\right)\mathbb{1} - i\sin\left(\varphi\right)\vec{n}\cdot\vec{\sigma} \tag{4.24}$$

In our case $\varphi = E\left(\theta\right)$ and therefore we can identify the quasienergy spectrum $\pm E\left(\theta\right)$ through:

$$E\left(\theta\right) = \arccos\left(\cos\left(K_1\right)\cos\left(K_2\right)\right) \tag{4.25}$$

Moreover, these considerations allow us to find expressions for the important quantities $\vec{n}_1(\theta)$ and $\vec{n}_2(\theta)$. Consequently we can then use our findings to calculate the winding numbers and with it the number of protected edge states.

$$n_{1,x} = \frac{\sin\left(K_1\right)\cos\left(K_2\right)}{\sin\left(E\right)} \qquad n_{1,y} = \frac{\sin\left(K_2\right)}{\sin\left(E\right)} \tag{4.26}$$

$$n_{2,x} = \frac{\sin\left(K_1\right)}{\sin\left(E\right)} \qquad n_{2,y} = \frac{\sin\left(K_2\right)\cos\left(K_1\right)}{\sin\left(E\right)} \tag{4.27}$$

Leaving us with the same result as shown in [22]. Let's now turn our attention to configurations of the DKQR where the gap in the quasienergy spectrum closes. These are of the outmost importance, because the topological invariant changes only when the gap closes. From this we can conclude, that topological phases (patches in configuration space with the same topological invariant) are seperated by configurations with a gapless spectrum. A gap closes if and only if:

$$\cos\left(K_1\right)\cos\left(K_2\right) = \pm 1 \tag{4.28}$$

Since we are dealing with a periodically driven system two gaps arise, one around zero energy and one around $\pi \equiv -\pi$ energy. In the case where the expression above is equal to one the zero energy gap closes, whereas the π energy gap closes when the expression is equal to negative one (this is due to the nature of the arccosine).

From the two chiral symmetric Floquet operators $\hat{U}_1$ and $\hat{U}_2$ we can deduce two winding numbers ν_1 and ν_2. As introduced previously:

$$\nu_l = \int_0^{2\pi} \frac{dx}{2\pi} \left(\vec{n}_l \times \frac{\partial\vec{n}_l(x)}{\partial x}\right)_3 \tag{4.29}$$

Note how closing a gap as described by (4.28) leads to $\vec{n}_1$ and $\vec{n}_2$ become indefinite (just throw a quick look at (4.26) and (4.27), a singularity arises) and the winding numbers are undefined.

4.1.3   Bulk Edge Correspondence

The winding numbers ν_1 and ν_2 are connected to the number of protected zero energy edge states ν_0 and the number of protected π energy edge states through:

$$\nu_0 = \frac{\nu_1 + \nu_2}{2} \tag{4.30}$$

$$\nu_\pi = \frac{\nu_1 - \nu_2}{2} \tag{4.31}$$

This equation holds, because zero energy edge states are on the same sublattice in both chiral symmetric time frames, but π energy edge states are on opposite ones[4].

4.2   Experiment

4.2.1   Mean Chiral Displacement

The topological invariant of the DKQR in the winding number is experimentally accessible thanks to an observable called "mean chiral displacement" or MCD, defined in [22]. In our case the definition boils down to the following expression:

$$C_l(t) = \langle \psi_{in}| \, \hat{U}_l^{-t} \left(\hat{n} \otimes -\sigma_z \right) \hat{U}_l^t \, |\psi_{in}\rangle \tag{4.32}$$

Note, that here we added an additional minus sign as compared to the proposal in [22], because this fixes an error in the sign made in the cited paper (more details under A.4.3). A short explanation for the minus sign is that we are dealing with momentum space instead of position space, like in most papers on topology in periodically driven systems. The l in the index differentiates between the Floquet operators $\hat{U}_1$ and $\hat{U}_2$. Averaging the mean chiral displacement over t steps in the time evolution gives us an expression that converges to the winding number:

$$\overline{C}_l(t) = \frac{1}{t} \sum_{t'=1}^{t} C_l(t') = \frac{\nu_l}{2} - \frac{1}{t} \sum_{t'=1}^{t} \int_{-\pi}^{\pi} \frac{d\theta}{2\pi} \frac{\cos\left(E(\theta)t\right)}{2} \left(\vec{n}_l \times \partial_\theta \vec{n}_l\right)_3$$

$$\xrightarrow{t \gg 1} \frac{\nu_l}{2} \tag{4.33}$$

The convergence stated holds, because with increasing t the term $\cos\left(E\left(\theta\right)t\right)$ oscillates faster and faster over the region of integration, as the dispersion relation $E\left(\theta\right)$ is not flat (consult equation (4.25)). Consequently, the second term $\left(\vec{n}_l \times \partial_\theta \vec{n}_l\right)_3$ is approximately constant on the scale of the fast oscillations and the integral over a periodic expression vanishes. More details under A.4.3

In the following subsections we will discuss a concrete implementation of the DQKR proposed and numerically simulate the system with regards to its ideal behaviour, as well as its behaviour under some unavoidable perturbations.

4.2.2   Experimental Difficulties

4.2.3   Setup

Building on the experimental realisation of QKR walks, as described in [6], and the proposed DKQR from [22] an experimental implementation of the periodically driven system discussed in this chapter might work as follows:

$$\hat{U} = \hat{M}\left(-\frac{\pi}{2}, \frac{\pi}{2}\right) \ \hat{T}_2 \ \hat{M}\left(\frac{\pi}{2}, \frac{\pi}{2}\right) \ \hat{M}\left(-\frac{\pi}{2}, 0\right) \ \hat{T}_1 \ \hat{M}\left(\frac{\pi}{2}, 0\right) = \hat{U}_{res} \tag{4.34}$$

$$\hat{T}_1 = e^{-ik_1 \cos\left(\hat{\theta}\right)\sigma_z} \tag{4.35}$$

$$\hat{T}_2 = e^{-ik_2 \sin\left(\hat{\theta}\right)\sigma_z} \tag{4.36}$$

Here $\hat{M}(\alpha, \chi)$ is the mixing matrix introduced in chapter 2, the rotations in spin space allow us to transforms spin orbit couplings in the x- and y-component (see equation (4.6)) to couplings in the z-component, discussed and implemented in the first two chapters. The combination of operators above equates to the Floquet operator (4.7) (proof in the appendix A.4.4) and the kicking through $\hat{T}_1$ can be performed the same way as in chapter 2. Whereas the second kick $\hat{T}_2$ can be realised by applying a second laser pulse proportional to $\sin(\theta)$ with amplitude k_2.

4.2.4   Numerical Simulation

Firstly, let us check the dependence of $\overline{C}_1(t)$ and $\overline{C}_2(t)$ on the kicking strengths k_1 and k_2 after $t = 20$ steps of the time evolution. To do so we fix $k_1 = \frac{\pi}{2}$ and vary k_2.
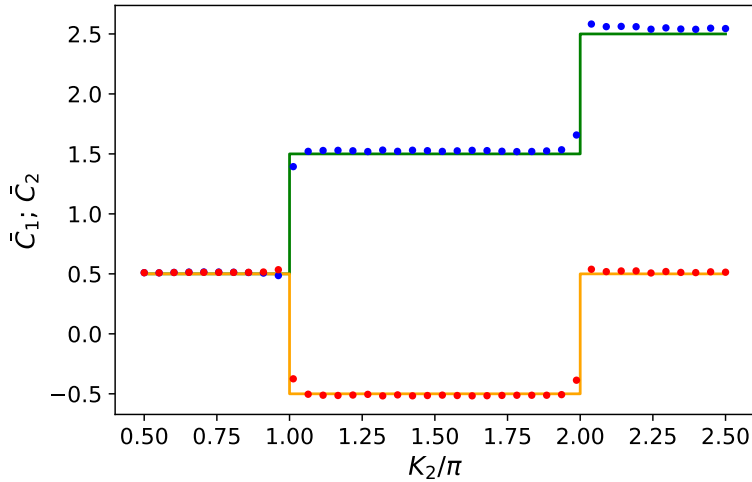
Figure 4.2: Ideal behaviour of the averged mean chiral displacement $\overline{C}_1(t)$ for the time evolution under $\hat{U}_1$ (in blue) and $\overline{C}_2(t)$ for the time evolution under $\hat{U}_2$ (in red). To check the convergence of $\overline{C}_1(t)$ towards $\frac{\nu_1}{2}$ and $\overline{C}_2(t)$ towards $\frac{\nu_2}{2}$ as stated in (4.29), $\frac{\nu_1}{2}$ in green and $\frac{\nu_2}{2}$ in yellow are plotted as well. The parameter $k_1 = \frac{\pi}{2}$ is kept constant at 40 values for k_2.

Twenty time evolution steps ensure a clear convergence while still being experimentally realisable, see the figure above depicting the ideal behaviour of the mean chiral

displacement.

Next up we include the kick-to-kick amplitude fluctuation previously discussed in chapter 2.
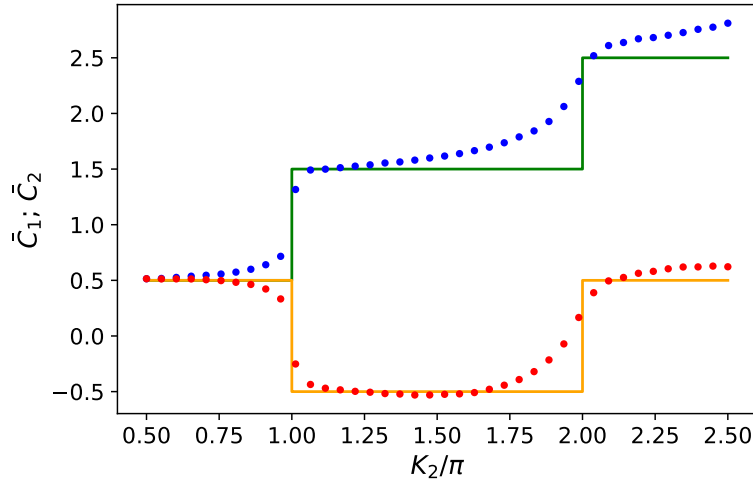
Figure 4.3: Kick-to-kick amplitude fluctuations of FWHM=$k \cdot 15\%$. Behaviour of the averged mean chiral displacement $\overline{C}_1(t)$ for the time evolution under $\hat{U}_1$ (in blue) and $\overline{C}_2(t)$ for the time evolution under $\hat{U}_2$ (in red). To check the convergence of $\overline{C}_1(t)$ towards $\frac{\nu_1}{2}$ and $\overline{C}_2(t)$ towards $\frac{\nu_2}{2}$ as stated in (4.29), $\frac{\nu_1}{2}$ in green and $\frac{\nu_2}{2}$ in yellow are plotted as well. The parameter $k_1 = \frac{\pi}{2}$ is kept constant at 40 values for k_2.

The average over 1000 trajectories is calculated by drawing random kicking strengths k_1 and k_2 according to the parameters of the gaussian distribution for every evolution step. For kick-to-kick amplitude flucatuations as expected to occur in the experiment (FWHM=$k \cdot 15\%$) the mean chiral displacement closely reflects the actual winding numbers, see figure 4.3. The connection between mean chiral displacement and topological invariants in the winding numbers is largely stable under amplitude fluctuations, but at transitions between topological phases (steps in the winding numbers) the perturbation becomes noticeable.

Another important perturbation affects the resonance condition of the DKQR, because the exact configuration $\beta = 0$ is experimentally inaccessible.
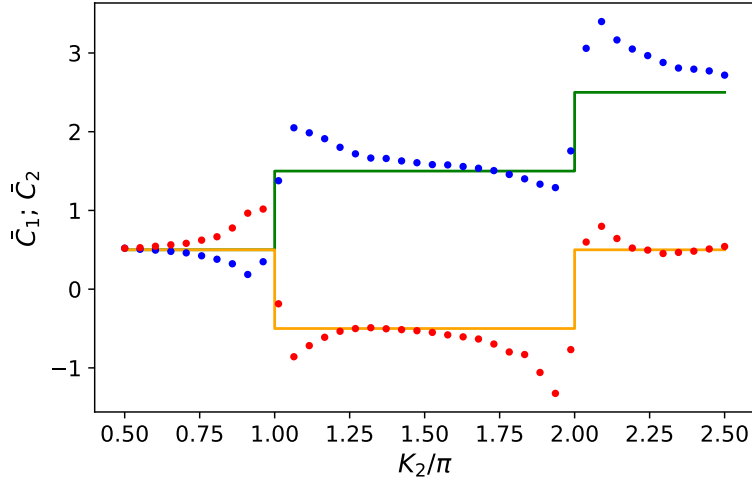
Figure 4.4: Quasimomentum distribution around $\beta = 0$ with $FWHM = 1\%$, average over 1000 trajectories. Behaviour of the averged mean chiral displacement $\overline{C}_1(t)$ for the time evolution under $\hat{U}_1$ (in blue) and $\overline{C}_2(t)$ for the time evolution under $\hat{U}_2$ (in red). To check the convergence of $\overline{C}_1(t)$ towards $\frac{\nu_1}{2}$ and $\overline{C}_2(t)$ towards $\frac{\nu_2}{2}$ as stated in (4.29), $\frac{\nu_1}{2}$ in green and $\frac{\nu_2}{2}$ in yellow are plotted as well. The parameter $k_1 = \frac{\pi}{2}$ is kept constant at 40 values for k_2.

Here the average over 1000 trajectories is calculated by drawing 1000 random betas according to the parameters of the gaussian distribution and keeping every drawn beta constant over the course of twenty steps. For large kicking strengths the connection between $\overline{C}_1$ and W_1 becomes imprecise, moreover around transitions between topological phases $\overline{C}_1$ and $\overline{C}_2$ deviate from W_1 and W_2. However $\overline{C}_1$ and $\overline{C}_2$ reflect W_1 and W_2 for configurations that are not close to topological phase transitions and do not feature large kicking strengths.

Lastly, the offresonant quasimomentum distribution and the kick-to-kick amplitude fluctuations will be simulated simultaneously. Just as before, 1000 random betas are drawn from a gaussian distribution and for every evolution step new random kicking strenghts k_1 and k_2 are applied.
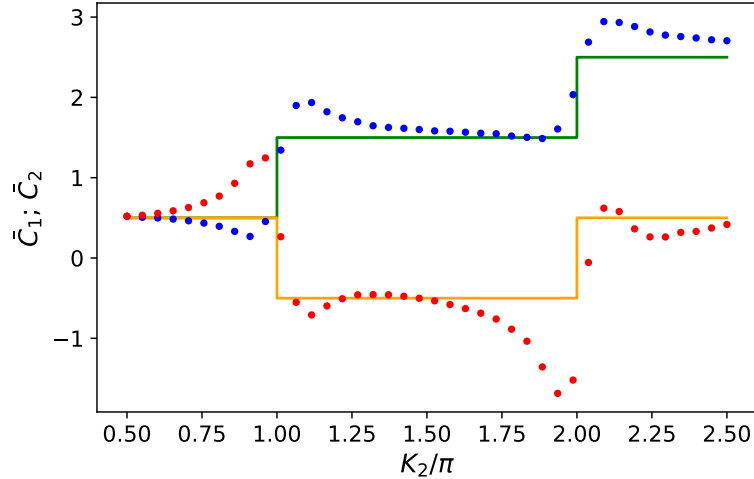
Figure 4.5: Quasimomentum distribution around $\beta = 0$ with $FWHM = 1\%$ and kick-to-kick amplitude fluctuations of FWHM=$k \cdot 10\%$, average over 1000 trajectories. Behaviour of the averged mean chiral displacement $\overline{C}_1(t)$ for the time evolution under $\hat{U}_1$ (in blue) and $\overline{C}_2(t)$ for the time evolution under $\hat{U}_2$ (in red). To check the convergence of $\overline{C}_1(t)$ towards $\frac{\nu_1}{2}$ and $\overline{C}_2(t)$ towards $\frac{\nu_2}{2}$ as stated in (4.29), $\frac{\nu_1}{2}$ in green and $\frac{\nu_2}{2}$ in yellow are plotted as well. The parameter $k_1 = \frac{\pi}{2}$ is kept constant at 40 values for k_2.

Combining relatively small perturbations in kick-to-kick amplitude fluctuations and offresonant quasimomentum, see figure 4.5, leads to a similar behaviour as seen in figure 4.4, for offresonant quasimomentum only. This suggests, that the connection between the mean chiral displacement and winding numbers is more sensitive to offresonant quasimomenta than to kick-to-kick amplitude fluctuations. In fact this discovery highlights the overarching importance of quantum resonance for the analysis of topological phases in the DKQR, as it is a fundamental presupposition on which the theory presented in this work builds. The quasimomentum distribution violates the quantum resonance condition and therefore has a strong perturbative effect, depicted in figure 4.4. In contrast to this the resonance condition is indepent of the kicking strength and consequently the perturbative effect of kick-to-kick amplitude fluctuations is smaller than that of the quasimomentum distribution.
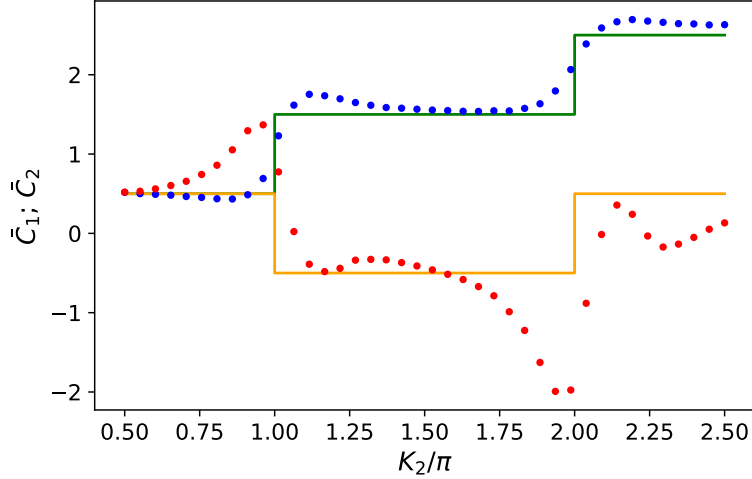
Figure 4.6: Quasimomentum distribution around $\beta = 0$ with $FWHM = 2\%$ and kick-to-kick amplitude fluctuations of FWHM=$k \cdot 15\%$, average over 1000 trajectories. Behaviour of the averged mean chiral displacement $\overline{C}_1(t)$ for the time evolution under $\hat{U}_1$ (in blue) and $\overline{C}_2(t)$ for the time evolution under $\hat{U}_2$ (in red). To check the convergence of $\overline{C}_1(t)$ towards $\frac{\nu_1}{2}$ and $\overline{C}_2(t)$ towards $\frac{\nu_2}{2}$ as stated in (4.29), $\frac{\nu_1}{2}$ in green and $\frac{\nu_2}{2}$ in yellow are plotted as well. The parameter $k_1 = \frac{\pi}{2}$ is kept constant at 40 values for k_2.

Figure 4.7: Quasimomentum distribution around $\beta = 0$ with $FWHM = 3\%$ and kick-to-kick amplitude fluctuations of FWHM=$k \cdot 30\%$, average over 1000 trajectories. Behaviour of the averged mean chiral displacement $\overline{C}_1(t)$ for the time evolution under $\hat{U}_1$ (in blue) and $\overline{C}_2(t)$ for the time evolution under $\hat{U}_2$ (in red). To check the convergence of $\overline{C}_1(t)$ towards $\frac{\nu_1}{2}$ and $\overline{C}_2(t)$ towards $\frac{\nu_2}{2}$ as stated in (4.29), $\frac{\nu_1}{2}$ in green and $\frac{\nu_2}{2}$ in yellow are plotted as well. The parameter $k_1 = \frac{\pi}{2}$ is kept constant at 40 values for k_2.

Stronger perturbations predominantly affect the connection between $\overline{C}_2$ and the winding number W_2, as they differ increasingly. On the other hand the connection between $\overline{C}_1$ and the winding number W_1 appears to be more stable, especially away

from topological phase transitions.

The kick-to-kick amplitude fluctuations introduce an additional complication in the light shift phase. In the experiment [7] the kick operators are realised in the following manner:

$$\hat{T}_1 = e^{-i2k_1 \cos^2\left(\frac{\theta}{2}\right)\sigma_z} = e^{-ik_1(\cos(\theta)+1)\sigma_z} \tag{4.37}$$

$$\hat{T}_2 = e^{-i2k_1 \cos^2\left(\frac{\theta}{2}-\frac{\pi}{2}\right)\sigma_z} = e^{-ik_2(\sin(\theta)+1)\sigma_z} \tag{4.38}$$

As the amplitude of every kick randomly fluctuates with $\triangle k_1, \triangle k_2$ the light shift phases $e^{-i\triangle k_1 \sigma_z}$ and $e^{-i\triangle k_2 \sigma_z}$ can not be compensated through an appropriate coin choice. Including the light shift phase in the simulation leads to the results below:
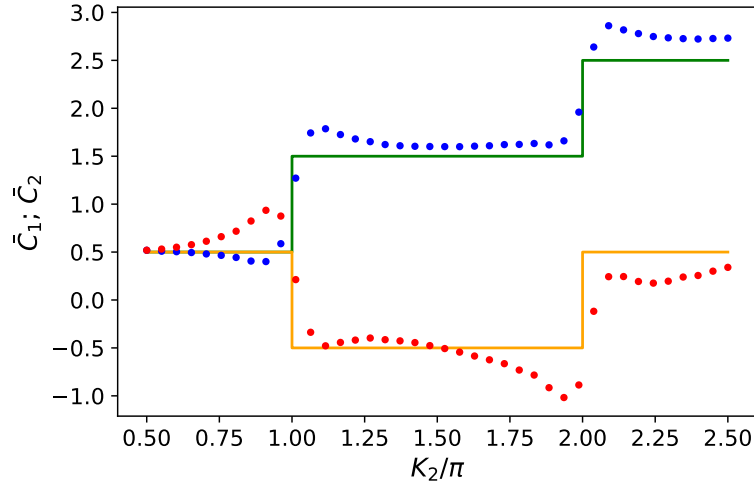
Figure 4.8: Quasimomentum distribution around $\beta = 0$ with $FWHM = 1\%$ and kick-to-kick amplitude fluctuations of FWHM=$k \cdot 15\%$, average over 1000 trajectories. Light shift phase included. Behaviour of the averged mean chiral displacement $\overline{C}_1(t)$ for the time evolution under $\hat{U}_1$ (in blue) and $\overline{C}_2(t)$ for the time evolution under $\hat{U}_2$ (in red). To check the convergence of $\overline{C}_1(t)$ towards $\frac{\nu_1}{2}$ and $\overline{C}_2(t)$ towards $\frac{\nu_2}{2}$ as stated in (4.29), $\frac{\nu_1}{2}$ in green and $\frac{\nu_2}{2}$ in yellow are plotted as well. The parameter $k_1 = \frac{\pi}{2}$ is kept constant at 40 values for k_2.

Figure 4.9: Quasimomentum distribution around $\beta = 0$ with $FWHM = 2\%$ and kick-to-kick amplitude fluctuations of FWHM=$k \cdot 20\%$, average over 1000 trajectories. Light shift phase included. Behaviour of the averged mean chiral displacement $\overline{C}_1(t)$ for the time evolution under $\hat{U}_1$ (in blue) and $\overline{C}_2(t)$ for the time evolution under $\hat{U}_2$ (in red). To check the convergence of $\overline{C}_1(t)$ towards $\frac{\nu_1}{2}$ and $\overline{C}_2(t)$ towards $\frac{\nu_2}{2}$ as stated in (4.29), $\frac{\nu_1}{2}$ in green and $\frac{\nu_2}{2}$ in yellow are plotted as well. The parameter $k_1 = \frac{\pi}{2}$ is kept constant at 40 values for k_2.
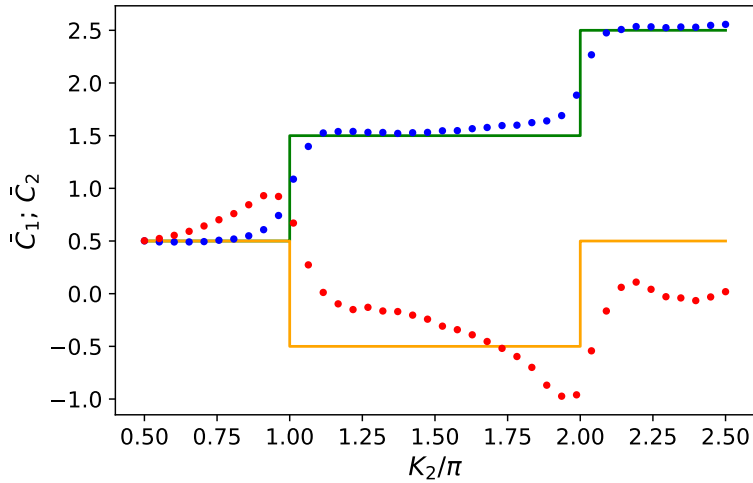
Figure 4.10: Quasimomentum distribution around $\beta = 0$ with $FWHM = 3\%$ and kick-to-kick amplitude fluctuations of FWHM=$k \cdot 30\%$, average over 1000 trajectories. Light shift phase included. Behaviour of the averged mean chiral displacement $\overline{C}_1(t)$ for the time evolution under $\hat{U}_1$ (in blue) and $\overline{C}_2(t)$ for the time evolution under $\hat{U}_2$ (in red). To check the convergence of $\overline{C}_1(t)$ towards $\frac{\nu_1}{2}$ and $\overline{C}_2(t)$ towards $\frac{\nu_2}{2}$ as stated in (4.29), $\frac{\nu_1}{2}$ in green and $\frac{\nu_2}{2}$ in yellow are plotted as well. The parameter $k_1 = \frac{\pi}{2}$ is kept constant at 40 values for k_2.

Figure 4.8 shows that the light shift phase does not destroy the convergence, only at large perturbations as in figure 4.10 the convergence is destroyed.
To summarise, the convergence of the mean chiral displacements towards the winding

numbers is exceptionally stable. Even under perturbations larger than those to be expected in the experiment, this statement is still valid (see figure 4.7), only at the transitions between different topological phases does a clear divergence arise.

Conclusion

Summary

In the course of this work we have established a new approach to the antiresonant configuration of the quantum kicked rotor, using a transformed Hamiltonian. In doing so, we have shown how the notion of different reference frames can help us better understand the implications of antiresonant configurations.

Additionally, we found that at a kicking strength of $k = 1.56$ the QKR walk best mimics the ideal quantum walk and we analysed the perturbative effects of quasi-momentum distribution, non-vanishing kickwidth and kick-to-kick amplitude fluctuations on the QKR walk.

After introducing the fundamentals for the study of topological phases, we went on to topologically classify the double kicked quantum rotor. We discovered, that the mean chiral displacements converges robustly towards the winding number of the system. Perturbations due to quasimomentum distribution and kick-to-kick amplitude fluctuations only had a notable effect at high kicking strengths and around topological phase transitions. Lastly, the quasimomentum distribution proved to have a more severe effect on the convergence than the kick-to-kick amplitude fluctuations, because it violates the quantum resonance condition.
Overall, the stability predominantly associated to topological phases also manifests in our study of the double kicked quantum rotor.

Outlook

In the future, a more detailed study of the protected edge states forming between regions of different topological invariants could be applied to the double kicked quantum rotor. By cutting links in the momentum space lattice two such regions might be established [22].

Firstly however, the theoretical and numerical results for the convergence of the mean chiral displacement towards the winding number in this work should be experimentally tested. In addition to the dominant perturbative effects treated here, the effect of decoherence through spontaneous emission could be explored.

Appendix A

Appendix

A.1 Quantum Kicked Rotor

A.1.1 Resonance Condition

The resonance condition has been stated in (1.9), now we will derive (1.10). First, let us eliminate the exponential:

$$\left(n^2 + 2n\beta\right) l \overset{!}{=} 2z \tag{A.1}$$

Here $z \in \mathbb{Z}$ is an arbitrary whole number and we used $\tau = 2\pi l$. Remember that, unless stated otherwise, the equations have to hold $\forall n \in \mathbb{Z}$. In the next step we make a case destinction, l has to be either even or odd. If l is even (A.1) can be reduced to:

$$2n\beta l \overset{!}{=} 2z' \Leftrightarrow n\beta l \overset{!}{=} z' \Rightarrow \beta = \frac{j}{l} \qquad\qquad j \in \{0, ..., l-1\} \tag{A.2}$$

Again $z' = z - \frac{n^2 l}{2} \in \mathbb{Z}$ is an arbitrary whole number. In the other case, where l is odd, we make an additional case destinction for n. If n is even, a similar argument as before holds:

$$2n\beta l \overset{!}{=} 2z' \overset{\text{n even}}{\Rightarrow} \beta = \frac{j}{2l} \qquad\qquad j \in \{0, ..., 2l-1\} \tag{A.3}$$

The definition of z' has not changed. Now n is odd:

$$2n\beta l \overset{!}{=} 2z' \Leftrightarrow n\beta l \overset{!}{=} z' \overset{\text{n odd}}{\Rightarrow} \beta = \frac{2j+1}{2l} \qquad\qquad j \in \{0, ..., l-1\} \tag{A.4}$$

So for l odd, β has to fulfill the right hand side of (A.3) and (A.4), which leaves us with the right hand side of (A.4) only.

All we have to do now, is to rewrite the conclusions in (A.2) and (A.4) in the form of (1.10). To achieve this we transform $j \to i = j - \frac{l}{2}$ for l even and $j \to i = j - \frac{l-1}{2}$ for l odd. Finally we are left with (1.10), for all $l \in \mathbb{N}$:

$$\beta = \frac{1}{2} + \frac{i}{l} \quad (\text{mod } 1) \qquad\qquad i \in \{0, ..., l-1\} \tag{A.5}$$

A.1.2   Energy Evolution

$$\langle E(K)\rangle = \langle\psi(K)|\,\hat{E}_{kin}\,|\psi(K)\rangle = \langle\psi(K)|\frac{\hat{p}^2}{2}\,|\psi(K)\rangle$$

$$= \int_0^{2\pi} \frac{1}{\sqrt{2\pi}}e^{-im\theta}e^{iK\cos(\theta)}\frac{1}{2}\left(-i\frac{\partial}{\partial\theta}\right)^2 e^{-iK\cos(\theta)}\frac{1}{\sqrt{2\pi}}e^{im\theta}d\theta$$

$$= \frac{-1}{4\pi}\int_0^{2\pi} e^{-im\theta}e^{iK\cos(\theta)}\left(\frac{\partial}{\partial\theta}\right)^2 e^{-iK\cos(\theta)}e^{im\theta}d\theta$$

$$= \frac{-1}{4\pi}\int_0^{2\pi} e^{-im\theta}e^{iK\cos(\theta)}\left(\frac{\partial}{\partial\theta}\right)\left[(iK\sin(\theta))+im\right]e^{-iK\cos(\theta)}e^{im\theta}d\theta$$

$$= \frac{-1}{4\pi}\int_0^{2\pi} e^{-im\theta}e^{iK\cos(\theta)}\left[(iK\sin(\theta))^2 + 2im\,(iK\sin(\theta))+(im)^2\right]e^{-iK\cos(\theta)}e^{im\theta}d\theta$$

$$= \frac{-1}{4\pi}\int_0^{2\pi} (iK\sin(\theta))^2 + (im)^2 d\theta$$

$$= \frac{K^2}{4}+\frac{m^2}{2} \tag{A.6}$$

It should be noted that we used the following inverse Fourier transform to find the representation of $|m\rangle$ in position space:

$$\psi_m(\theta) = \frac{1}{\sqrt{2\pi}}\int_{-\infty}^{\infty}\delta(p-m)e^{ip\theta}dp = \frac{1}{\sqrt{2\pi}}e^{im\theta} \tag{A.7}$$

A.1.3   Simple Quantum Ratchet

Here we are considering the resonant case $\beta = 0$ and $\tau = 4\pi$.

$$\langle p(K,\phi)\rangle = \langle\psi(K,\phi)|\,\hat{p}\,|\psi(K,\phi)\rangle$$

$$= \frac{1}{2\pi}\int_0^{2\pi}\frac{1}{\sqrt{2}}\left(1+e^{i\phi}e^{-i\theta}\right)e^{iK\cos(\theta)}\left(-i\frac{\partial}{\partial\theta}+\beta\right)e^{-iK\cos(\theta)}\frac{1}{\sqrt{2}}\left(1+e^{-i\phi}e^{i\theta}\right)d\theta$$

$$= \frac{1}{4\pi}\int_0^{2\pi}\left(1+e^{-i(\theta-\phi)}\right)e^{iK\cos(\theta)}$$

$$\left[(-i)\,(iK\sin(\theta))\,e^{-iK\cos(\theta)}\cdot\left(1+e^{i(\theta-\phi)}\right)+(-i)e^{-iK\cos(\theta)}\cdot ie^{i(\theta-\phi)}\right]d\theta$$

$$= \frac{1}{4\pi}\int_0^{2\pi}\left(1+e^{-i(\theta-\phi)}\right)\left[K\sin(\theta)\cdot\left(1+e^{i(\theta-\phi)}\right)+e^{i(\theta-\phi)}\right]d\theta$$

$$= \frac{1}{4\pi}\int_0^{2\pi}K\sin(\theta)\left(2+e^{i(\theta-\phi)}+e^{-i(\theta-\phi)}\right)+e^{i(\theta-\phi)}+1\,d\theta$$

$$= \frac{1}{4\pi}\int_0^{2\pi}1+2K\cos(\theta-\phi)\sin(\theta)d\theta = \frac{1}{2}+2K\left[\frac{1}{4}\left(2\theta\sin(\phi)-\cos(2\theta-\phi)\right)\right]_0^{2\pi}$$

$$= \frac{1}{2}+\frac{K}{2}\sin(\phi) \tag{A.8}$$

A.1.4   Transformation of the Schrödinger equation

In this subsection a detailed proof for the equivalence of the two Schrödinger equations used in 1.1.4 will be given. Again, we are considering the antiresonant case

only!
The definitions we will be using and the statement we want to prove revisited:

$$\psi(x,t) \rightarrow \ \psi'(x,t) = \hat{G}\,\psi(x,t) = e^{-i\beta(\hat{p}t-2\hat{x})}\psi(x,t) \tag{A.9}$$

$$\hat{H} = \frac{\hat{p}^2}{2} + k\cos\left(\hat{x}\right) \cdot \sum_{n=0}^{\infty} \delta(t-n\tau) \tag{A.10}$$

$$\hat{H}' = \frac{1}{2}\left(\hat{p}-2\beta\right)^2 + \beta\hat{p} + \cos\left(\hat{x}\right) \cdot \sum_{n=0}^{\infty}(-1)^n\delta(t-n\tau) \tag{A.11}$$

$$\hat{H}\psi(x,t) = i\partial_t\psi(x,t) \Longleftrightarrow \hat{H}'\psi'(x,t) = i\partial_t\psi'(x,t) \tag{A.12}$$

In order to prove (A.12) first we use (A.9) to simplify the statement and to make the task in front of us more clear:

$$\hat{H} - i\partial_t = \hat{G}^\dagger\left[\hat{H}' - i\partial_t\right]\hat{G} \tag{A.13}$$

Let us start by looking at the time derivative:

$$-i\partial_t\hat{G} = -i\left(\hat{G}\partial_t - i\beta\hat{p}\hat{G}\right) = \hat{G}(-i\partial_t) + \beta\hat{p}\hat{G} \tag{A.14}$$

Next up are all terms in $\hat{H}'$ containing $\hat{p}$:

$$\left(\frac{1}{2}\left(\hat{p}-2\beta\right)^2 + \beta\hat{p}\right)\hat{G} = \frac{1}{2}\left(\hat{p}^2 - 4\beta\hat{p} + 4\beta^2\right)\hat{G} + \beta\hat{p}\hat{G}$$

$$= \frac{1}{2}\left(4\beta^2\hat{G} - 4\beta(\hat{G}\hat{p} + 2\beta\hat{G}) + \hat{p}(\hat{G}\hat{p} + 2\beta\hat{G})\right) + \beta\hat{p}\hat{G}$$

$$= 2\beta^2\hat{G} - 2\beta\hat{G}\hat{p} - 4\beta^2\hat{G} + \frac{1}{2}\left(\hat{G}\hat{p} + 2\beta\hat{G}\right)\hat{p} + \beta\left(\hat{G}\hat{p} + 2\beta\hat{G}\right) + \beta\hat{p}\hat{G}$$

$$= 2\beta^2\hat{G} - 2\beta\hat{G}\hat{p} - 4\beta^2\hat{G} + \frac{\hat{G}\hat{p}^2}{2} + \beta\hat{G}\hat{p} + \beta\hat{G}\hat{p} + 2\beta^2\hat{G} + \beta\hat{p}\hat{G}$$

$$= \frac{\hat{G}\hat{p}^2}{2} + \beta\hat{p}\hat{G} \tag{A.15}$$

The last step left is to commutate $\hat{G}$ with the delta-kicking potential:

$$\left(k\cos\left(\hat{x}\right)\cdot\sum_{n=0}^{\infty}(-1)^n\delta(t-n\tau)\right)\hat{G} = \left(\frac{k}{2}\left(e^{i\hat{x}} + e^{-i\hat{x}}\right)\cdot\sum_{n=0}^{\infty}(-1)^n\delta(t-n\tau)\right)\hat{G}$$

$$= \left(e^{i\hat{x}} + e^{-i\hat{x}}\right)\hat{G}\,\frac{k}{2}\cdot\sum_{n=0}^{\infty}(-1)^n\delta(t-n\tau) \tag{A.16}$$

We will ignore the factors which commutate with $\hat{G}$ for better clarity. Here we use the Campbell-Baker-Hausdorff formula to commutate the operators:

$$\left(e^{i\hat{x}} + e^{-i\hat{x}}\right)\hat{G} = \left(e^{i\hat{x}} + e^{-i\hat{x}}\right)e^{-i\beta(\hat{p}t-\hat{x})}$$

$$= e^{-i\beta(\hat{p}t-\hat{x})}e^{i\hat{x}}e^{[i\hat{x},-i\beta(\hat{p}t-\hat{x})]} + e^{-i\beta(\hat{p}t-\hat{x})}e^{-i\hat{x}}e^{[-i\hat{x},-i\beta(\hat{p}t-\hat{x})]}$$

$$= e^{-i\beta(\hat{p}t-\hat{x})}e^{i\hat{x}}e^{-i\beta t} + e^{-i\beta(\hat{p}t-\hat{x})}e^{-i\hat{x}}e^{i\beta t}$$

$$= \hat{G}e^{i\hat{x}}e^{-i\beta t} + \hat{G}e^{-i\hat{x}}e^{i\beta t} \tag{A.17}$$

The Campbell-Baker-Hausdorff formula holds, because $[\hat{x},[\hat{x},\hat{p}]] = [\hat{p},[\hat{p},\hat{x}]] = 0$. With the result (A.17) we return to (A.16):

$$\hat{G}\left(e^{i\hat{x}}e^{-i\beta t} + e^{-i\hat{x}}e^{i\beta t}\right)\frac{k}{2}\cdot\sum_{n=0}^{\infty}(-1)^{n}\delta(t-n\tau)$$

$$= \hat{G}\frac{k}{2}\cdot\sum_{n=0}^{\infty}\left(e^{i\hat{x}}e^{-i\beta t} + e^{-i\hat{x}}e^{i\beta t}\right)(-1)^{n}\delta(t-n\tau)$$

$$= \hat{G}\frac{k}{2}\cdot\sum_{n=0}^{\infty}\left(e^{i\hat{x}}e^{-i\beta\tau n} + e^{-i\hat{x}}e^{i\beta\tau n}\right)(-1)^{n}\delta(t-n\tau) \tag{A.18}$$

We choose $\tau = 4\pi f$ with $f \in \mathbb{N}$. To cancel out the factor $(-1)^{n}$, which is the characteristic of antiresonance, the following condition has to be satisfied:

$$\beta\tau \overset{!}{=} \pi \quad (\mathrm{mod}\ 2\pi) \tag{A.19}$$

$$\beta = \frac{2i+1}{4f} \qquad\qquad i \in \{0,...,2f-1\} \tag{A.20}$$

Back to (A.18), we can use this information:

$$\hat{G}\frac{k}{2}\cdot\sum_{n=0}^{\infty}\left(e^{i\hat{x}}e^{-i\pi n} + e^{-i\hat{x}}e^{i\pi n}\right)(-1)^{n}\delta(t-n\tau)$$

$$= \hat{G}\frac{k}{2}\cdot\sum_{n=0}^{\infty}\left(e^{i\hat{x}}(-1)^{n} + e^{-i\hat{x}}(-1)^{n}\right)(-1)^{n}\delta(t-n\tau)$$

$$= \hat{G}\frac{k}{2}\cdot\sum_{n=0}^{\infty}\left(e^{i\hat{x}} + e^{-i\hat{x}}\right)\delta(t-n\tau)$$

$$= \hat{G}k\cos(\hat{x})\cdot\sum_{n=0}^{\infty}\delta(t-n\tau) \tag{A.21}$$

Now we can combine the results (A.14), (A.15) and (A.21), inserting them into the right hand side of (A.13) gives:

$$\hat{G}^{\dagger}\left[\hat{H}' - i\partial_t\right]\hat{G} = \hat{G}^{\dagger}\left[\hat{G}\frac{\hat{p}^2}{2} + \beta\hat{p}\hat{G} + \hat{G}k\cos(\hat{x})\cdot\sum_{n=0}^{\infty}\delta(t-n\tau) - \hat{G}i\partial_t - \beta\hat{p}\hat{G}\right]$$

$$= \frac{\hat{p}^2}{2} + k\cos(\hat{x})\cdot\sum_{n=0}^{\infty}\delta(t-n\tau) - i\partial_t$$

$$= \hat{H} - i\partial_t \tag{A.22}$$

This concludes the proof. We have shown the two Schrödinger equations to be equivalent in antiresonance.

A.2 QKR Walks

A.2.1 Step operator

Here we will reformulate the step operator in a more approachable fashion:

$$
\begin{aligned}
\hat{S} &= \exp\left(-i\frac{\tau}{2}\hat{p}^2 \otimes \mathbb{1}\right) \cdot \exp\left(-ik\cos\left(\hat{\theta}\right) \otimes 2\hat{S}_z\right) \\
&= \exp\left(-i\frac{\tau}{2}\hat{p}^2 \otimes \mathbb{1}\right) \cdot \sum_{m=0}^{\infty} \frac{1}{m!}\left(-ik\cos\left(\hat{\theta}\right) \otimes 2\hat{S}_z\right)^m \\
&= \exp\left(-i\frac{\tau}{2}\hat{p}^2 \otimes \mathbb{1}\right) \cdot \sum_{m=0}^{\infty} \frac{1}{m!}\left(-ik\cos\left(\hat{\theta}\right)\right)^m \otimes \left(2\hat{S}_z\right)^m \\
&\equiv \exp\left(-i\frac{\tau}{2}\hat{p}^2 \otimes \mathbb{1}\right) \cdot \sum_{m=0}^{\infty} \frac{1}{m!}\left(-ik\cos\left(\hat{\theta}\right)\right)^m \cdot \begin{pmatrix} 1 & 0 \\ 0 & -1 \end{pmatrix}^m \\
&= \exp\left(-i\frac{\tau}{2}\hat{p}^2\right) \cdot \begin{pmatrix} \exp\left(-ik\cos\left(\hat{\theta}\right)\right) & 0 \\ 0 & \exp\left(ik\cos\left(\hat{\theta}\right)\right) \end{pmatrix}
\end{aligned} \tag{A.23}
$$

A.2.2 Time evolution after two kicks

The time evolution operators representing two kicks will be derived explicitly for the resonant and antiresonant case.

$$
\begin{aligned}
\hat{W}_{anti} &= \left(\mathbb{1} \otimes \hat{C}\right)\hat{S}_{anti}\left(\mathbb{1} \otimes \hat{C}\right)\hat{S}_{anti} \\
&\equiv \frac{1}{2}\begin{pmatrix} 1 & i \\ i & 1 \end{pmatrix} e^{-i\pi\hat{n}}\begin{pmatrix} e^{-ik\cos(\hat{\theta})} & 0 \\ 0 & e^{ik\cos(\hat{\theta})} \end{pmatrix}\begin{pmatrix} 1 & i \\ i & 1 \end{pmatrix} e^{-i\pi\hat{n}}\begin{pmatrix} e^{-ik\cos(\hat{\theta})} & 0 \\ 0 & e^{ik\cos(\hat{\theta})} \end{pmatrix} \\
&= \frac{1}{2}\begin{pmatrix} 1 & i \\ i & 1 \end{pmatrix} e^{-i\pi\hat{n}}\begin{pmatrix} e^{-ik\cos(\hat{\theta})} & ie^{-ik\cos(\hat{\theta})} \\ ie^{ik\cos(\hat{\theta})} & e^{ik\cos(\hat{\theta})} \end{pmatrix} e^{-i\pi\hat{n}}\begin{pmatrix} e^{-ik\cos(\hat{\theta})} & 0 \\ 0 & e^{ik\cos(\hat{\theta})} \end{pmatrix} \\
&= \frac{1}{2}\begin{pmatrix} 1 & i \\ i & 1 \end{pmatrix}\begin{pmatrix} e^{ik\cos(\hat{\theta})} & ie^{ik\cos(\hat{\theta})} \\ ie^{-ik\cos(\hat{\theta})} & e^{-ik\cos(\hat{\theta})} \end{pmatrix}\begin{pmatrix} e^{-ik\cos(\hat{\theta})} & 0 \\ 0 & e^{ik\cos(\hat{\theta})} \end{pmatrix} \\
&= \frac{1}{2}\begin{pmatrix} 1 & i \\ i & 1 \end{pmatrix}\begin{pmatrix} 1 & ie^{2ik\cos(\hat{\theta})} \\ ie^{-2ik\cos(\hat{\theta})} & 1 \end{pmatrix} \\
&= \frac{1}{2}\begin{pmatrix} 1 - e^{-2ik\cos(\hat{\theta})} & i\left(1 + e^{2ik\cos(\hat{\theta})}\right) \\ i\left(1 + e^{-2ik\cos(\hat{\theta})}\right) & 1 - e^{2ik\cos(\hat{\theta})} \end{pmatrix}
\end{aligned} \tag{A.24}
$$

In the next to last step the translation explained in 1.1.4 was applied and the coin used is still Y, defined in (2.3). Now for the resonant case:

$$\hat{W}_{res} = \left(\mathbb{1} \otimes \hat{C}\right) \hat{S}_{res} \left(\mathbb{1} \otimes \hat{C}\right) \hat{S}_{res}$$

$$\equiv \frac{1}{2} \begin{pmatrix} 1 & i \\ i & 1 \end{pmatrix} \begin{pmatrix} e^{-ik\cos(\hat{\theta})} & 0 \\ 0 & e^{ik\cos(\hat{\theta})} \end{pmatrix} \begin{pmatrix} 1 & i \\ i & 1 \end{pmatrix} \begin{pmatrix} e^{-ik\cos(\hat{\theta})} & 0 \\ 0 & e^{ik\cos(\hat{\theta})} \end{pmatrix}$$

$$= \frac{1}{2} \begin{pmatrix} 1 & i \\ i & 1 \end{pmatrix} \begin{pmatrix} e^{-ik\cos(\hat{\theta})} & ie^{-ik\cos(\hat{\theta})} \\ ie^{ik\cos(\hat{\theta})} & e^{ik\cos(\hat{\theta})} \end{pmatrix} \begin{pmatrix} e^{-ik\cos(\hat{\theta})} & 0 \\ 0 & e^{ik\cos(\hat{\theta})} \end{pmatrix}$$

$$= \frac{1}{2} \begin{pmatrix} 1 & i \\ i & 1 \end{pmatrix} \begin{pmatrix} e^{-2ik\cos(\hat{\theta})} & i \\ i & e^{2ik\cos(\hat{\theta})} \end{pmatrix}$$

$$= \frac{1}{2} \begin{pmatrix} e^{-2ik\cos(\hat{\theta})} - 1 & i\left(1 + e^{2ik\cos(\hat{\theta})}\right) \\ i\left(1 + e^{-2ik\cos(\hat{\theta})}\right) & e^{2ik\cos(\hat{\theta})} - 1 \end{pmatrix} \tag{A.25}$$

A.2.3 Transformation in Antiresonance

Here a more detailed calculation of $\hat{W}'_{anti}$ will be stated.

$$\hat{W}'_{anti} = \hat{R}^\dagger \hat{W}_{anti} \hat{R}$$

$$\equiv \begin{pmatrix} -i & 0 \\ 0 & i \end{pmatrix} \frac{1}{2} \begin{pmatrix} 1 - e^{-2ik\cos(\hat{\theta})} & i\left(1 + e^{2ik\cos(\hat{\theta})}\right) \\ i\left(1 + e^{-2ik\cos(\hat{\theta})}\right) & 1 - e^{2ik\cos(\hat{\theta})} \end{pmatrix} \begin{pmatrix} i & 0 \\ 0 & -i \end{pmatrix}$$

$$= \begin{pmatrix} -i & 0 \\ 0 & i \end{pmatrix} \frac{1}{2} \begin{pmatrix} 1 - a & i(1 + a^*) \\ i(1 + a) & 1 - a^* \end{pmatrix} \begin{pmatrix} i & 0 \\ 0 & -i \end{pmatrix}$$

$$= \frac{1}{2} \begin{pmatrix} -i & 0 \\ 0 & i \end{pmatrix} \begin{pmatrix} i(1 - a) & 1 + a^* \\ -1 - a & -i(1 - a^*) \end{pmatrix}$$

$$= \frac{1}{2} \begin{pmatrix} 1 - a & -i(1 + a^*) \\ -i(1 + a) & 1 - a^* \end{pmatrix}$$

$$= \frac{1}{2} \begin{pmatrix} 1 - e^{-2ik\cos(\hat{\theta})} & -i\left(1 + e^{2ik\cos(\hat{\theta})}\right) \\ -i\left(1 + e^{-2ik\cos(\hat{\theta})}\right) & 1 - e^{2ik\cos(\hat{\theta})} \end{pmatrix} = -\hat{W}_{res} \tag{A.26}$$

For better clarity the substitution $a = e^{-2ik\cos(\hat{\theta})}$ has been used.

A.2.4 Explicit Calculation of momentum distribution

The aim in this subsection is to calculate the momentum distribution after the operation "kick-free evolution-coin-kick-free evolution" in resonance and antiresonance for the same initial wavefunction and compare the results, because the theory developed in 2.1.2 tells us the should be identical.

$$|\psi_{in}\rangle = \frac{1}{2} \left(|1\rangle + |2\rangle\right) \otimes \left(|n = 0\rangle - i |n = 1\rangle\right) = \frac{1}{\sqrt{2}} \left(|1\rangle + |2\rangle\right) \otimes |\psi_r\rangle \tag{A.27}$$

We refer to the operation "kick-free evolution-coin-kick-free evolution" by $\hat{A}_{res}$ in resonance and by $\hat{A}_{anti}$ in antiresonance. These operators are the same as $\hat{W}_{res}$ and $\hat{W}_{anti}$ with applying the coin one time less:

$$
\begin{aligned}
\hat{A}_{anti} &= e^{-i\pi\hat{n}} \begin{pmatrix} e^{-ik\cos(\hat{\theta})} & 0 \\ 0 & e^{ik\cos(\hat{\theta})} \end{pmatrix} \frac{1}{\sqrt{2}} \begin{pmatrix} 1 & i \\ i & 1 \end{pmatrix} e^{-i\pi\hat{n}} \begin{pmatrix} e^{-ik\cos(\hat{\theta})} & 0 \\ 0 & e^{ik\cos(\hat{\theta})} \end{pmatrix} \\
&= \frac{1}{\sqrt{2}} \begin{pmatrix} e^{ik\cos(\hat{\theta})} & ie^{ik\cos(\hat{\theta})} \\ ie^{-ik\cos(\hat{\theta})} & e^{-ik\cos(\hat{\theta})} \end{pmatrix} \begin{pmatrix} e^{-ik\cos(\hat{\theta})} & 0 \\ 0 & e^{ik\cos(\hat{\theta})} \end{pmatrix} \\
&= \frac{1}{\sqrt{2}} \begin{pmatrix} 1 & ie^{2ik\cos(\hat{\theta})} \\ ie^{-2ik\cos(\hat{\theta})} & 1 \end{pmatrix}
\end{aligned}
\tag{A.28}
$$

$$
\begin{aligned}
\hat{A}_{res} &= \frac{1}{\sqrt{2}} \begin{pmatrix} e^{-ik\cos(\hat{\theta})} & ie^{-ik\cos(\hat{\theta})} \\ ie^{ik\cos(\hat{\theta})} & e^{ik\cos(\hat{\theta})} \end{pmatrix} \begin{pmatrix} e^{-ik\cos(\hat{\theta})} & 0 \\ 0 & e^{ik\cos(\hat{\theta})} \end{pmatrix} \\
&= \frac{1}{\sqrt{2}} \begin{pmatrix} e^{-2ik\cos(\hat{\theta})} & i \\ i & e^{2ik\cos(\hat{\theta})} \end{pmatrix}
\end{aligned}
\tag{A.29}
$$

Now let us determine how $\hat{A}_{res}$ and $\hat{A}_{anti}$ affect the system, hence we will apply them to an initial wavefunction, where $|\psi_r\rangle = \frac{1}{\sqrt{2}} (|n=0\rangle - i\,|n=1\rangle)$ signifies a ratchet state.

$$
\hat{A}_{res} |\psi_{in}\rangle = \frac{1}{2} \begin{pmatrix} i + e^{-2ik\cos(\hat{\theta})} \\ i + e^{2ik\cos(\hat{\theta})} \end{pmatrix} |\psi_r\rangle = \frac{i}{2} \begin{pmatrix} 1 - ie^{-2ik\cos(\hat{\theta})} \\ 1 - ie^{2ik\cos(\hat{\theta})} \end{pmatrix} |\psi_r\rangle
\tag{A.30}
$$

$$
\hat{A}_{anti} |\psi_{in}\rangle = \frac{1}{2} \begin{pmatrix} 1 + ie^{2ik\cos(\hat{\theta})} \\ 1 + ie^{-2ik\cos(\hat{\theta})} \end{pmatrix} |\psi_r\rangle
\tag{A.31}
$$

We want to check the momentum distribution for the result in (A.30):

$$
\begin{aligned}
\left| \langle n| \hat{A}_{res} |\psi_{in}\rangle \right|^2 &= \frac{1}{4} \left| \langle n| \left(1 - i \sum_{m=-\infty}^{\infty} (-i)^m e^{-im\hat{\theta}} J_m(2k) \right) |\psi_r\rangle \right|^2 \\
&\quad + \frac{1}{4} \left| \langle n| \left(1 + i \sum_{m=-\infty}^{\infty} (-i)^m e^{-im\hat{\theta}} (-1)^m J_m(2k) \right) |\psi_r\rangle \right|^2
\end{aligned}
\tag{A.32}
$$

Here we used the Jacobi-Anger identity and the fact that $J_m(-x) = (-1)^m J_m(x)$ applies for Bessel functions of the first kind. On the right hand side we can identify two contributions to the momentum distribution, each of them corresponds to one hyperfine state ($|1\rangle$ or $|2\rangle$). To make our calculations more compact, we will only consider the contribution by $|1\rangle$:

$$\frac{1}{4}\left|\langle n|\left[\frac{1}{\sqrt{2}}\left(|n=0\rangle - i\,|n=1\rangle\right) - i\sum_m (-i)^m J_m(2k)\frac{1}{\sqrt{2}}\left(|n=m\rangle - i\,|n=m+1\rangle\right)\right]\right|^2$$

$$=\frac{1}{4}\left[\frac{1}{\sqrt{2}}\left(\langle n|n=0\rangle - i\,\langle n|n=1\rangle\right) - i\sum_m (-i)^m J_m(2k)\frac{1}{\sqrt{2}}\left(\langle n|n=m\rangle - i\,\langle n|n=m+1\rangle\right)\right]$$

$$\left[\frac{1}{\sqrt{2}}\left(\langle n|n=0\rangle + i\,\langle n|n=1\rangle\right) + i\sum_m (i)^m J_m(2k)\frac{1}{\sqrt{2}}\left(\langle n|n=m\rangle + i\,\langle n|n=m+1\rangle\right)\right]$$

$$=\frac{1}{4}\left[\frac{1}{\sqrt{2}}\left(\delta_{n,0} - i\delta_{n,1}\right) - i\sum_m (-i)^m J_m(2k)\frac{1}{\sqrt{2}}\left(\delta_{n,m} - i\delta_{n,m+1}\right)\right]$$

$$\left[\frac{1}{\sqrt{2}}\left(\delta_{n,0} + i\delta_{n,1}\right) + i\sum_m (i)^m J_m(2k)\left(\delta_{n,m} + i\delta_{n,m+1}\right)\right]$$

$$=\frac{1}{4}\frac{1}{\sqrt{2}}\left[\left(\delta_{n,0} - i\delta_{n,1}\right) - i\sum_m (-i)^m J_m(2k)\left(\delta_{n,m} - i\delta_{n,m+1}\right)\right]$$

$$\left[\left(\delta_{n,0} + i\delta_{n,1}\right) + i\sum_m (-i)^m(-1)^m J_m(2k)\left(\delta_{n,m} + i\delta_{n,m+1}\right)\right]$$

$$=\frac{1}{4}\frac{1}{\sqrt{2}}[2 + iJ_0(2k) + ii(-1)J_{-1}(2k)i - ii(-i)(-1)J_1(2k) - iiJ_0(2k)i$$

$$- iJ_0(2k) - iiJ_{-1}(2k)(-i) + i(-i)(-i)J_1(2k) + i(-i)J_0(2k)(-i)$$

$$+ \left(-i\sum_m (-i)^m J_m(2k)\left(\delta_{n,m} - i\delta_{n,m+1}\right)\right)\cdot\left(i\sum_m (-i)^m(-1)^m J_m(2k)\left(\delta_{n,m} + i\delta_{n,m+1}\right)\right)]$$

$$=\frac{1}{4}\frac{1}{\sqrt{2}}\left[2 + \left(-i\sum_m (-i)^m J_m(2k)\left(\delta_{n,m} - i\delta_{n,m+1}\right)\right)\cdot\left(i\sum_m (-i)^m(-1)^m J_m(2k)\left(\delta_{n,m} + i\delta_{n,m+1}\right)\right)\right]$$

$$(A.33)$$

An analogous calculation (again we consider only the contribution from $|1\rangle$) departing from equation (A.31) gives:

$$\frac{1}{4}\left|\langle n|\left[\frac{1}{\sqrt{2}}\left(|n=0\rangle - i\,|n=1\rangle\right) + i\sum_m (-i)^m(-1)^m J_m(2k)\frac{1}{\sqrt{2}}\left(|n=m\rangle - i\,|n=m+1\rangle\right)\right]\right|^2$$

$$=\frac{1}{4}\frac{1}{\sqrt{2}}\left[2 + \left(i\sum_m (-i)^m(-1)^m J_m(2k)\left(\delta_{n,m} - i\delta_{n,m+1}\right)\right)\cdot\left(-i\sum_m (-i)^m J_m(2k)\left(\delta_{n,m} + i\delta_{n,m+1}\right)\right)\right]$$

$$(A.34)$$

The same calculation can be carried out for the contribution by $|2\rangle$ and because both contributions to the momentum distribution are the same regardless of resonance or antiresonance, the result is in accordance with the theory developed previously in 2.1.2.

A.2.5 Kick-to-Kick Amplitude Fluctuations

In this subsection additional results from the numerical simulation of kick-to-kick amplitude fluctuations will be presented.

(a) $FWHM = k \cdot 20\%$ (b) $FWHM = k \cdot 80\%$
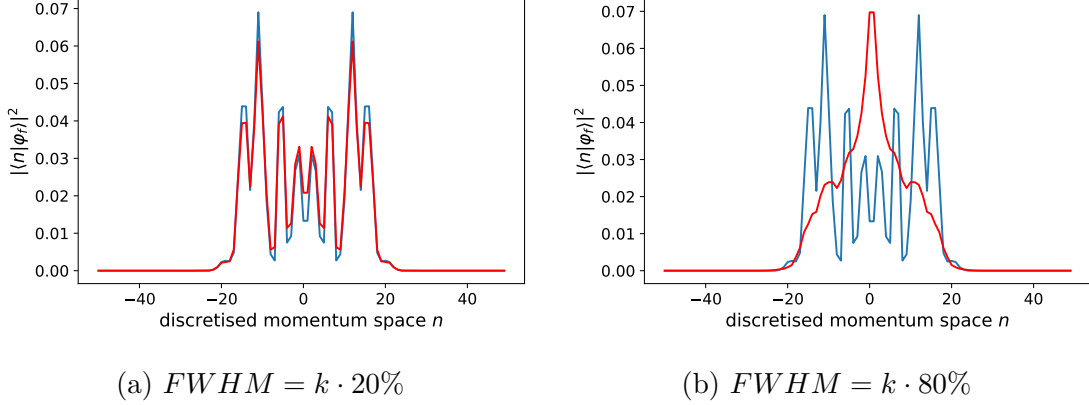
Figure A.1: Comparison between the ideal case (in blue) and the case where every kickstrength is drawn from a normal distribution with the mentioned full width at half maximum (in red), average over 2000 trajectories

A.2.6 Arbitrary Mixing

In a spin-1/2 system a general spinor can be written as follows:

$$\begin{pmatrix} r_1 e^{i\varphi_1} \\ r_2 e^{i\varphi_2} \end{pmatrix} = \begin{pmatrix} r_1 e^{i\varphi_1} \\ \sqrt{1-r_1^2}\,e^{i\varphi_2} \end{pmatrix} \equiv \begin{pmatrix} r_1 \\ \sqrt{1-r_1^2}\,e^{i(\varphi_2-\varphi_1)} \end{pmatrix} = \begin{pmatrix} r_1 \\ \sqrt{1-r_1^2}\,e^{i\phi} \end{pmatrix} \qquad (A.35)$$

We want to prove that through the application of $\hat{M}(\alpha,\chi)$ any spinor can be transformed into any other spinor. It suffices to show this property for the basis consisting of $|\uparrow\rangle$ and $|\downarrow\rangle$:

$$\hat{M}(\alpha,\chi)\,|\uparrow\rangle \equiv \begin{pmatrix} \cos\left(\frac{\alpha}{2}\right) & e^{-i\chi}\sin\left(\frac{\alpha}{2}\right) \\ -e^{i\chi}\sin\left(\frac{\alpha}{2}\right) & \cos\left(\frac{\alpha}{2}\right) \end{pmatrix} \begin{pmatrix} 1 \\ 0 \end{pmatrix}$$

$$= \begin{pmatrix} \cos\left(\frac{\alpha}{2}\right) \\ -\sin\left(\frac{\alpha}{2}\right)e^{i\chi} \end{pmatrix} \overset{!}{=} \begin{pmatrix} r_1 \\ \sqrt{1-r_1^2}\,e^{i\phi} \end{pmatrix} \qquad (A.36)$$

This equation is statisfied for the choice $\alpha = 2\arccos(r_1)$ and $\phi = \chi - \pi$.

$$\hat{M}(\alpha,\chi)\,|\downarrow\rangle \equiv \begin{pmatrix} \cos\left(\frac{\alpha}{2}\right) & e^{-i\chi}\sin\left(\frac{\alpha}{2}\right) \\ -e^{i\chi}\sin\left(\frac{\alpha}{2}\right) & \cos\left(\frac{\alpha}{2}\right) \end{pmatrix} \begin{pmatrix} 0 \\ 1 \end{pmatrix}$$

$$= \begin{pmatrix} \sin\left(\frac{\alpha}{2}\right)e^{-i\chi} \\ \cos\left(\frac{\alpha}{2}\right) \end{pmatrix} \overset{!}{=} \begin{pmatrix} r_1 \\ \sqrt{1-r_1^2}\,e^{i\phi} \end{pmatrix} \equiv \begin{pmatrix} r_1 e^{-i\phi} \\ \sqrt{1-r_1^2} \end{pmatrix} \qquad (A.37)$$

This equation is statisfied for the choice $\alpha = 2\arccos(r_1)$ and $\phi = \chi$, we used the fact that global phases can be neglected.

A.3   Topological study

A.3.1   Energy eigenvalues

To identify all the energy eigenvalues it suffices to solve the following equation for λ:

$$0 \overset{!}{=} \det\left(\hat{H}_{em} - \lambda \cdot \mathbb{1}\right) \tag{A.38}$$

$$\Leftrightarrow 0 = \lambda^2 - |H|^2$$
$$\Leftrightarrow 0 = (\lambda - H)(\lambda + H)$$
$$\Rightarrow \lambda_{1,2} = \pm H \tag{A.39}$$

An analogous computation for $\hat{H}'_{em}$ reveals:

$$0 \overset{!}{=} \det\left(\hat{H}'_{em} - \lambda \cdot \mathbb{1}\right) \tag{A.40}$$

$$\Leftrightarrow 0 = \lambda^2 - 2\lambda V + V^2 - |H|^2$$
$$\Leftrightarrow 0 = (\lambda + V - H)(\lambda + V + H)$$
$$\Rightarrow \lambda_{1,2} = V \pm H \tag{A.41}$$

A.4   Double Kicked Quantum Rotor

A.4.1   Naiv approach

For simplicitiy's sake we definde $\kappa = k\cos(\theta)$.

$$\hat{U} = \left(\mathbb{1} \otimes \hat{Y}\right) \cdot \hat{S} \equiv \frac{1}{\sqrt{2}}\begin{pmatrix} 1 & i \\ i & 1 \end{pmatrix} e^{-ik\cos(\theta)\sigma_x}$$

$$= \frac{1}{\sqrt{2}}\begin{pmatrix} 1 & i \\ i & 1 \end{pmatrix}\begin{pmatrix} \cos(\kappa) & -i\sin(\kappa) \\ -i\sin(\kappa) & \cos(\kappa) \end{pmatrix}$$

$$= \frac{1}{\sqrt{2}}\begin{pmatrix} \cos(\kappa)+\sin(\kappa) & i\cos(\kappa)-i\sin(\kappa) \\ i\cos(\kappa)-i\sin(\kappa) & \cos(\kappa)+\sin(\kappa) \end{pmatrix} \tag{A.42}$$

In the third step we used the following relation:

$$e^{-i\kappa\vec{n}\cdot\vec{\sigma}} = \mathbb{1}\cdot\cos(\kappa) - i\sin(\kappa)\,\vec{n}\cdot\vec{\sigma} \tag{A.43}$$

Now let's check chiral symmetry:

$$\hat{\Gamma}^\dagger\hat{U}\hat{\Gamma} = \hat{\Gamma}\hat{U}\hat{\Gamma}$$

$$= \frac{1}{\sqrt{2}}\begin{pmatrix} 1 & 0 \\ 0 & -1 \end{pmatrix}\begin{pmatrix} \cos(\kappa)+\sin(\kappa) & i\cos(\kappa)-i\sin(\kappa) \\ i\cos(\kappa)-i\sin(\kappa) & \cos(\kappa)+\sin(\kappa) \end{pmatrix}\begin{pmatrix} 1 & 0 \\ 0 & -1 \end{pmatrix}$$

$$= \frac{1}{\sqrt{2}}\begin{pmatrix} \cos(\kappa)+\sin(\kappa) & i\cos(\kappa)-i\sin(\kappa) \\ -i\cos(\kappa)+i\sin(\kappa) & -\cos(\kappa)-\sin(\kappa) \end{pmatrix} = \hat{U}^\dagger \tag{A.44}$$

A.4.2 Chiral symmetric timeframes

Now we want to prove the chiral symmetry of $\hat{U}_1$ and $\hat{U}_2$ with regards to $\hat{\Gamma} \equiv \mathbb{1} \otimes \sigma_z$:

$$\hat{\Gamma}^\dagger e^{-iK_1(\hat{\theta})\sigma_x} \hat{\Gamma} \equiv \begin{pmatrix} 1 & 0 \\ 0 & -1 \end{pmatrix} \begin{pmatrix} \cos(K_1) & -i\sin(K_1) \\ -i\sin(K_1) & \cos(K_1) \end{pmatrix} \begin{pmatrix} 1 & 0 \\ 0 & -1 \end{pmatrix}$$

$$= \begin{pmatrix} \cos(K_1) & -i\sin(K_1) \\ i\sin(K_1) & -\cos(K_1) \end{pmatrix} \begin{pmatrix} 1 & 0 \\ 0 & -1 \end{pmatrix}$$

$$= \begin{pmatrix} \cos(K_1) & i\sin(K_1) \\ i\sin(K_1) & \cos(K_1) \end{pmatrix} \equiv e^{iK_1(\hat{\theta})\sigma_x}$$

$$\hat{\Gamma}^\dagger e^{-iK_2(\hat{\theta})\sigma_y} \hat{\Gamma} \equiv \begin{pmatrix} 1 & 0 \\ 0 & -1 \end{pmatrix} \begin{pmatrix} \cos(K_2) & -\sin(K_2) \\ \sin(K_2) & \cos(K_2) \end{pmatrix} \begin{pmatrix} 1 & 0 \\ 0 & -1 \end{pmatrix}$$

$$= \begin{pmatrix} \cos(K_2) & -\sin(K_2) \\ -\sin(K_2) & -\cos(K_2) \end{pmatrix} \begin{pmatrix} 1 & 0 \\ 0 & -1 \end{pmatrix}$$

$$= \begin{pmatrix} \cos(K_2) & \sin(K_2) \\ -\sin(K_2) & \cos(K_2) \end{pmatrix} \equiv e^{iK_2(\hat{\theta})\sigma_y}$$

$$\Rightarrow \hat{\Gamma}^\dagger \hat{U}_1 \hat{\Gamma} = \hat{\Gamma}^\dagger e^{-i\frac{1}{2}K_1(\hat{\theta})\sigma_x} e^{-iK_2(\hat{\theta})\sigma_y} e^{-i\frac{1}{2}K_1(\hat{\theta})\sigma_x} \hat{\Gamma}$$

$$= e^{i\frac{1}{2}K_1(\hat{\theta})\sigma_x} e^{iK_2(\hat{\theta})\sigma_y} e^{i\frac{1}{2}K_1(\hat{\theta})\sigma_x} = \hat{U}_1^\dagger \tag{A.45}$$

$$\Rightarrow \hat{\Gamma}^\dagger \hat{U}_2 \hat{\Gamma} = \hat{\Gamma}^\dagger e^{-i\frac{1}{2}K_2(\hat{\theta})\sigma_y} e^{-iK_1(\hat{\theta})\sigma_x} e^{-i\frac{1}{2}K_2(\hat{\theta})\sigma_y} \hat{\Gamma}$$

$$= e^{i\frac{1}{2}K_2(\hat{\theta})\sigma_y} e^{iK_1(\hat{\theta})\sigma_x} e^{i\frac{1}{2}K_2(\hat{\theta})\sigma_y} = \hat{U}_2^\dagger \tag{A.46}$$

$$\tag{A.47}$$

The fact that $\sigma_x \to -\sigma_x$ and $\sigma_y \to -\sigma_y$ under the application of $\hat{\Gamma} \equiv \sigma_z$ is expected, because $\hat{\Gamma}$ can be interpreted as a rotation in spin-space by π around the z-axis (neglecting a factor of i as a global phase). This concludes the proof of chiral symmetry for $\hat{U}_1$ and $\hat{U}_2$, an important ingredient for the topological analysis to be carried out.

Let's derive the matrix representation of $\hat{U}_1$ and $\hat{U}_2$, as it will prove to be very useful. We want to calculate the following products:

$$\hat{U}_1 \equiv e^{-i\frac{1}{2}K_1(\hat{\theta})\sigma_x} e^{-iK_2(\hat{\theta})\sigma_y} e^{-i\frac{1}{2}K_1(\hat{\theta})\sigma_x}$$

$$= \begin{pmatrix} \cos\left(\frac{K_1}{2}\right) & -i\sin\left(\frac{K_1}{2}\right) \\ -i\sin\left(\frac{K_1}{2}\right) & \cos\left(\frac{K_1}{2}\right) \end{pmatrix} \begin{pmatrix} \cos(K_2) & -\sin(K_2) \\ \sin(K_2) & \cos(K_2) \end{pmatrix} \begin{pmatrix} \cos\left(\frac{K_1}{2}\right) & -i\sin\left(\frac{K_1}{2}\right) \\ -i\sin\left(\frac{K_1}{2}\right) & \cos\left(\frac{K_1}{2}\right) \end{pmatrix}$$

$$\hat{U}_2 \equiv e^{-i\frac{1}{2}K_2(\hat{\theta})\sigma_y} e^{-iK_1(\hat{\theta})\sigma_x} e^{-i\frac{1}{2}K_2(\hat{\theta})\sigma_y} \tag{A.48}$$

$$= \begin{pmatrix} \cos\left(\frac{K_2}{2}\right) & -\sin\left(\frac{K_2}{2}\right) \\ \sin\left(\frac{K_2}{2}\right) & \cos\left(\frac{K_2}{2}\right) \end{pmatrix} \begin{pmatrix} \cos(K_1) & -i\sin(K_1) \\ -i\sin(K_1) & \cos(K_1) \end{pmatrix} \begin{pmatrix} \cos\left(\frac{K_2}{2}\right) & -\sin\left(\frac{K_2}{2}\right) \\ \sin\left(\frac{K_2}{2}\right) & \cos\left(\frac{K_2}{2}\right) \end{pmatrix}$$

$$\tag{A.49}$$

Firstly consider $\hat{U}_1$ and calculate the matrix elements one by one:

$$\hat{U}_1 \equiv e^{-i\frac{1}{2}K_1(\hat{\theta})\sigma_x} e^{-iK_2(\hat{\theta})\sigma_y} e^{-i\frac{1}{2}K_1(\hat{\theta})\sigma_x}$$

$$= \begin{pmatrix} \cos\left(\frac{K_1}{2}\right) & -i\sin\left(\frac{K_1}{2}\right) \\ -i\sin\left(\frac{K_1}{2}\right) & \cos\left(\frac{K_1}{2}\right) \end{pmatrix} \begin{pmatrix} \cos\left(K_2\right) & -\sin\left(K_2\right) \\ \sin\left(K_2\right) & \cos\left(K_2\right) \end{pmatrix} \begin{pmatrix} \cos\left(\frac{K_1}{2}\right) & -i\sin\left(\frac{K_1}{2}\right) \\ -i\sin\left(\frac{K_1}{2}\right) & \cos\left(\frac{K_1}{2}\right) \end{pmatrix}$$

$$\Rightarrow U_{1,1} = \cos\left(K_2\right)\cos^2\left(\frac{K_1}{2}\right) + i\sin\left(K_2\right)\sin\left(\frac{K_1}{2}\right)\cos\left(\frac{K_1}{2}\right)$$

$$- i\sin\left(K_2\right)\cos\left(\frac{K_1}{2}\right)\sin\left(\frac{K_1}{2}\right) - \cos\left(K_2\right)\sin^2\left(\frac{K_1}{2}\right)$$

$$= \cos\left(K_2\right)\cos\left(K_1\right)$$

$$U_{1,2} = -i\cos\left(K_2\right)\cos\left(\frac{K_1}{2}\right)\sin\left(\frac{K_1}{2}\right) + \sin\left(K_2\right)\sin^2\left(\frac{K_1}{2}\right)$$

$$+ \sin\left(K_2\right)\cos^2\left(\frac{K_1}{2}\right) - i\cos\left(K_2\right)\sin\left(\frac{K_1}{2}\right)\cos\left(\frac{K_1}{2}\right)$$

$$= \sin\left(K_2\right) - i\cos\left(K_2\right)\sin\left(K_1\right)$$

$$U_{2,1} = -i\cos\left(K_2\right)\cos\left(\frac{K_1}{2}\right)\sin\left(\frac{K_1}{2}\right) - \sin\left(K_2\right)\sin^2\left(\frac{K_1}{2}\right)$$

$$- \sin\left(K_2\right)\cos^2\left(\frac{K_1}{2}\right) - i\cos\left(K_2\right)\sin\left(\frac{K_1}{2}\right)\cos\left(\frac{K_1}{2}\right)$$

$$= -\sin\left(K_2\right) - i\cos\left(K_2\right)\sin\left(K_1\right)$$

$$U_{2,2} = -\cos\left(K_2\right)\sin^2\left(\frac{K_1}{2}\right) + i\sin\left(K_2\right)\sin\left(\frac{K_1}{2}\right)\cos\left(\frac{K_1}{2}\right)$$

$$- i\sin\left(K_2\right)\cos\left(\frac{K_1}{2}\right)\sin\left(\frac{K_1}{2}\right) + \cos\left(K_2\right)\cos^2\left(\frac{K_1}{2}\right)$$

$$= \cos\left(K_2\right)\cos\left(K_1\right)$$

$$\Rightarrow \hat{U}_1 \equiv \begin{pmatrix} \cos\left(K_2\right)\cos\left(K_1\right) & -\sin\left(K_2\right) - i\cos\left(K_2\right)\sin\left(K_1\right) \\ \sin\left(K_2\right) - i\cos\left(K_2\right)\sin\left(K_1\right) & \cos\left(K_2\right)\cos\left(K_1\right) \end{pmatrix} \quad \text{(A.50)}$$

The same process can be repeated for $\hat{U}_2$:

$$
\begin{aligned}
\hat{U}_2 &\equiv e^{-i\frac{1}{2}K_2(\hat{\theta})\sigma_y} e^{-iK_1(\hat{\theta})\sigma_x} e^{-i\frac{1}{2}K_2(\hat{\theta})\sigma_y} \\
&= \begin{pmatrix} \cos\left(\frac{K_2}{2}\right) & -\sin\left(\frac{K_2}{2}\right) \\ \sin\left(\frac{K_2}{2}\right) & \cos\left(\frac{K_2}{2}\right) \end{pmatrix} \begin{pmatrix} \cos\left(K_1\right) & -i\sin\left(K_1\right) \\ -i\sin\left(K_1\right) & \cos\left(K_1\right) \end{pmatrix} \begin{pmatrix} \cos\left(\frac{K_2}{2}\right) & -\sin\left(\frac{K_2}{2}\right) \\ \sin\left(\frac{K_2}{2}\right) & \cos\left(\frac{K_2}{2}\right) \end{pmatrix} \\
&= \begin{pmatrix} \cos\left(K_2\right)\cos\left(K_1\right) & -\sin\left(K_2\right)\cos\left(K_1\right)-i\sin\left(K_1\right) \\ \sin\left(K_2\right)\cos\left(K_1\right)-i\sin\left(K_1\right) & \cos\left(K_2\right)\cos\left(K_1\right) \end{pmatrix}
\end{aligned} \tag{A.51}
$$

A.4.3 Mean Chiral Displacement and Winding Numbers

In this subsection the mistake made in [22] will be discussed. We begin with:

$$
C_l(t) = \langle \psi_{in}| \, \hat{U}_l^{-t} \left(\hat{n} \otimes -\sigma_z \right) \hat{U}_l^t \, |\psi_{in}\rangle \tag{A.52}
$$

At this point it is important to note that:

$$
\hat{n} = -i\partial_\theta \tag{A.53}
$$

In the proof however the substitution $\hat{n} = i\partial_\theta$ is made. The proof is discussed in detail in [22] and [14].

A.4.4 Experimental Setup

Here a proof for equation (4.34) will be provided:

$$
\begin{aligned}
\hat{U} &= \hat{M}\left(-\frac{\pi}{2},\frac{\pi}{2}\right) \; \hat{T}_2 \; \hat{M}\left(\frac{\pi}{2},\frac{\pi}{2}\right) \; \hat{M}\left(-\frac{\pi}{2},0\right) \; \hat{T}_1 \; \hat{M}\left(\frac{\pi}{2},0\right) \\
&= \exp\left(i\frac{\pi}{4}\sigma_x\right) \hat{T}_2 \exp\left(-i\frac{\pi}{4}\sigma_x\right) \exp\left(i\frac{\pi}{4}\sigma_y\right) \hat{T}_1 \exp\left(-i\frac{\pi}{4}\sigma_y\right) \\
&= e^{-ik_2\sin(\hat{\theta})\sigma_y} e^{-ik_1\cos(\hat{\theta})\sigma_x} = \hat{U}_{res}
\end{aligned} \tag{A.54}
$$

A rotation in spin space was applied to the following operators:

$$
\hat{T}_1 = e^{-ik_1\cos(\hat{\theta})\sigma_z} \tag{A.55}
$$

$$
\hat{T}_2 = e^{-ik_2\sin(\hat{\theta})\sigma_z} \tag{A.56}
$$

Bibliography

[1]   Y. Aharonov, L. Davidovich, and N. Zagury. "Quantum random walks". In: *Phys. Rev. A* 48 (2 Aug. 1993), pp. 1687–1690. DOI: 10.1103/PhysRevA.48. 1687. URL: https://link.aps.org/doi/10.1103/PhysRevA.48.1687.

[2]   Anton Akhmerov. "Topology and symmetry". In: (2014). URL: https:// topocondmat.org/w1_topointro/0d.html.

[3]   Jeeva Anandan. "The geometric phase". In: *Nature* 360.6402 (1992), p. 307.

[4]   János K. Asbóth and Hideaki Obuse. "Bulk-boundary correspondence for chiral symmetric quantum walks". In: *Phys. Rev. B* 88 (12 Sept. 2013), p. 121406. DOI: 10.1103/PhysRevB.88.121406. URL: https://link.aps.org/doi/10. 1103/PhysRevB.88.121406.

[5]   János K Asbóth, László Oroszlány, and András Pályi. "A Short Course on Topological Insulators". In: *Lecture Notes in Physics* 919 (2016). URL: https: //arxiv.org/pdf/1509.02295.pdf.

[6]   Siamak Dadras et al. "Quantum Walk in Momentum Space with a Bose-Einstein Condensate". In: *Phys. Rev. Lett.* 121 (7 Aug. 2018), p. 070402. DOI: 10.1103/PhysRevLett.121.070402. URL: https://link.aps.org/doi/10. 1103/PhysRevLett.121.070402.

[7]   C Groiseau, A Gresch, and S Wimberger. "Quantum walks of kicked Bose–Einstein condensates". In: *Journal of Physics A: Mathematical and Theoretical* 51.27 (2018), p. 275301. URL: http://stacks.iop.org/1751-8121/51/i=27/a= 275301.

[8]   A. J. Heeger et al. "Solitons in conducting polymers". In: *Rev. Mod. Phys.* 60 (3 July 1988), pp. 781–850. DOI: 10.1103/RevModPhys.60.781. URL: https://link.aps.org/doi/10.1103/RevModPhys.60.781.

[9]   Martin Holthaus. "Floquet engineering with quasienergy bands of periodically driven optical lattices". In: *Journal of Physics B: Atomic, Molecular and Optical Physics* 49.1 (2016), p. 013001. URL: http://stacks.iop.org/0953-4075/49/i=1/a=013001.

[10]   Julia Kempe. "Quantum random walks: an introductory overview". In: *Contemporary Physics* 44.4 (2003), pp. 307–327. URL: https://arxiv.org/pdf/ quant-ph/0303081.pdf.

[11]   Takuya Kitagawa et al. "Exploring topological phases with quantum walks". In: *Phys. Rev. A* 82 (3 Sept. 2010), p. 033429. DOI: 10.1103/PhysRevA.82. 033429. URL: https://link.aps.org/doi/10.1103/PhysRevA.82.033429.

[12] K. v. Klitzing, G. Dorda, and M. Pepper. "New Method for High-Accuracy Determination of the Fine-Structure Constant Based on Quantized Hall Resistance". In: *Phys. Rev. Lett.* 45 (6 Aug. 1980), pp. 494–497. DOI: 10.1103/PhysRevLett.45.494. URL: https://link.aps.org/doi/10.1103/PhysRevLett.45.494.

[13] J M Kosterlitz and D J Thouless. "Ordering, metastability and phase transitions in two-dimensional systems". In: *Journal of Physics C: Solid State Physics* 6.7 (1973), p. 1181. URL: http://stacks.iop.org/0022-3719/6/i=7/a=010.

[14] Maria Maffei et al. "Topological characterization of chiral models through their long time dynamics". In: *New Journal of Physics* 20.1 (2018), p. 013023. URL: http://stacks.iop.org/1367-2630/20/i=1/a=013023.

[15] F. L. Moore et al. "Atom Optics Realization of the Quantum δ-Kicked Rotor". In: *Phys. Rev. Lett.* 75 (25 Dec. 1995), pp. 4598–4601. DOI: 10.1103/PhysRevLett.75.4598. URL: https://link.aps.org/doi/10.1103/PhysRevLett.75.4598.

[16] Shinsei Ryu et al. "Topological insulators and superconductors: tenfold way and dimensional hierarchy". In: *New Journal of Physics* 12.6 (2010), p. 065010. URL: http://stacks.iop.org/1367-2630/12/i=6/a=065010.

[17] Mark Sadgrove et al. "Scaling law and stability for a noisy quantum system". In: *Phys. Rev. E* 78 (2 Aug. 2008), p. 025206. DOI: 10.1103/PhysRevE.78.025206. URL: https://link.aps.org/doi/10.1103/PhysRevE.78.025206.

[18] Jacob Shapiro. "The Bulk-Edge Correspondence in Three Simple Cases". In: *arXiv preprint arXiv:1710.10649* (2017). URL: https://arxiv.org/pdf/1710.10649.pdf.

[19] Neil Shenvi, Julia Kempe, and K. Birgitta Whaley. "Quantum random-walk search algorithm". In: *Phys. Rev. A* 67 (5 May 2003), p. 052307. DOI: 10.1103/PhysRevA.67.052307. URL: https://link.aps.org/doi/10.1103/PhysRevA.67.052307.

[20] Gil Summy and Sandro Wimberger. "Quantum random walk of a Bose-Einstein condensate in momentum space". In: *Phys. Rev. A* 93 (2 Feb. 2016), p. 023638. DOI: 10.1103/PhysRevA.93.023638. URL: https://link.aps.org/doi/10.1103/PhysRevA.93.023638.

[21] Sandro Wimberger, Italo Guarneri, and Shmuel Fishman. "Quantum resonances and decoherence for δ-kicked atoms". In: *Nonlinearity* 16.4 (2003), p. 1381. URL: http://stacks.iop.org/0951-7715/16/i=4/a=312.

[22] Longwen Zhou and Jiangbin Gong. "Floquet topological phases in a spin-1/2 double kicked rotor". In: *Phys. Rev. A* 97 (6 June 2018), p. 063603. DOI: 10.1103/PhysRevA.97.063603. URL: https://link.aps.org/doi/10.1103/PhysRevA.97.063603.

Erklärung

Ich versichere, dass ich diese Arbeit selbstständig verfasst und keine anderen als die angegebenen Quellen und Hilfsmittel benutzt habe.

Heidelberg, den 29 November 2018,